JGR Atmospheres

RESEARCH ARTICLE
10.1029/2022JD038153

Key Points:
- Hyperspectral radiances are efficiently compressed into a limited number of uncorrelated parameters: the Transformed Retrievals (TRs)
- Assimilation of TRs is akin to assimilation of physical profiles
- The assimilation of TRs results in a higher forecast accuracy in predicting the distribution of the water vapor

Correspondence to:
T. Cherubini,
tiziana@hawaii.edu

Citation:
Cherubini, T., Antonelli, P., Businger, S., & Scaccia, P. (2023). Assimilation of Transformed Retrievals from satellite high-resolution infrared data over the Central Pacific Area. *Journal of Geophysical Research: Atmospheres*, *128*, e2022JD038153. https://doi.org/10.1029/2022JD038153

Received 9 NOV 2022
Accepted 22 MAY 2023

Assimilation of Transformed Retrievals From Satellite High-Resolution Infrared Data Over the Central Pacific Area

Tiziana Cherubini[1], Paolo Antonelli[2], Steven Businger[1], and Paolo Scaccia[2]

[1]Department of Atmospheric Sciences, Mauna Kea Weather Center, University of Hawaii, Honolulu, HI, USA, [2]AdaptiveMeteo S.r.l., Roma, Italy

Abstract A month-long data assimilation experiment is carried out to assess the impact of CrIS and IASI Transformed Retrievals (TRs) on the accuracy of analyses and forecasts from a 3-hr Weather Research and Forecasting cycling system implemented over the central North Pacific Ocean. Conventional observations and satellite MicroWave (MW) radiance data are assimilated along with TRs in comparative experiments. Both the NCEP Global Forecasting System and the European Centre for Medium-Range Weather Forecasts analyses are used in the evaluation process. The results show that the assimilation of TRs alone, and in combination with MW radiance assimilation, have the greatest impact on the characterization of the moisture field in the middle atmospheric levels (800–300 hPa), and particularly in the lower portion (800–600 hPa). The latter improvement is likely due to a refinement in the vertical definition of the trade-wind inversion.

Plain Language Summary A month-long data assimilation experiment is carried out to assess the impact of hyper-spectral sensor Transformed Retrievals (TRs) on the accuracy of analyses and forecasts from a 3-hr Weather Research and Forecasting cycling system implemented over the central North Pacific Ocean. TRs are the result of a mathematical inversion process that compresses the informational content of the hyper-spectral radiances into a limited number of uncorrelated parameters, and provides an ad hoc observation operator, for their assimilation within Numerical Weather Prediction models. Conventional observations and satellite MicroWave (MW) radiance data are assimilated along with TRs in comparative experiments. Both the NCEP Global Forecasting System and the European Centre for Medium-Range Weather Forecasts analyses are used in the evaluation process. The results show that the assimilation of TRs, both alone, and in combination with MW radiance assimilation, have the greatest impact on the characterization of the moisture field in the middle atmospheric levels (800–300 hPa), and particularly in the lower portion (800–600 hPa). The latter improvement is likely due to a refinement in the vertical definition of the trade-wind inversion.

1. Introduction

Current Numerical Weather Prediction (NWP) data assimilation systems only use a limited number of channels from high spectral resolution InfraRed instruments, known as hyperspectral IR, and assimilation of cloudy observations is further restricted to an even smaller number of channels (McNally, 2009). Alternative assimilation techniques based on Principal Component Analysis compression have also faced limitations due to trace gases and aerosol contaminated atmospheric components (Matricardi & McNally, 2014). However, with the increasing number of hyperspectral IR instruments flown on polar platforms and the future launch of the Meteosat Third Generation InfraRed Sounder on a geostationary platform, more efficient techniques for information content extraction and assimilation into NWP systems are necessary.

Migliorini et al. (2008) and Migliorini (2012) provided a framework to assimilate hyperspectral IR data in an equivalent way to direct radiance assimilation by mapping the data into physical retrievals and transforming them via a partial eigen-decomposition to exploit the null-space filtered effect (Joiner & Da Silva, 1998; Rodgers, 2000). Inspired by this work, a 1DVAR inversion system called Mirto was developed (Antonelli et al., 2017, A2017 hereafter) capable of generating Transformed Retrievals (TRs), that is, the projections of the hyperspectral IR observations onto the eigen-vectors space. TRs represent the highest form of compression of the hyperspectral sensors' observations. Assimilation of TRs into NPW system has several advantages including overcoming errors introduced by using an a priori knowledge of the atmospheric state in the physical retrieval process (Eyre, 2007; Eyre et al., 2019), efficiency in processing thousands of wavelengths available from hyperspectral instruments, independence from the characteristics of the instruments, and the ability to include wavelengths corresponding to trace gases like ozone and carbon dioxide (A2017).

This paper presents the results of an assessment on the impact of assimilating TRs into the Weather Research and Forecasting (WRF) modeling system during a month-long experiment over the Central North Pacific Area. This study builds on the work by Antonelli et al. (2020, A2020 hereafter) where TRs were generated using Mirto and ingested into the WRF model (Skamarock et al., 2008), via a modified version of the 3DVAR data assimilation system (WRFDA, Barker et al., 2004, 2012). Preliminary results in A2020 were encouraging and showed a positive impact on the characterization of the water vapor distribution, and a decrease in the root mean square error (RMS) of the 3-hr accumulated precipitation forecasts for the record-breaking Kauai flood event (Corrigan & Businger, 2021). These preliminary results from a limited case study prompted the present more comprehensive assessment study.

Since A2017, the retrieval processor, Mirto, was refined and extended to be able to retrieve profiles above the cloud top, greatly expanding the TRs assimilation potential in cloudy regions such as higher latitudes in winter. However, assimilation of TRs above the cloud top is not mature enough to be included in this study. The current investigation expands on A2020 in two ways: (a) includes a month-long assimilation experiment that allows for robust forecast statistics and (b) independently assimilates MicroWave (MW) radiance observations into the WRFDA system (Barker et al., 2004, 2012). The MW emissions from atmospheric water vapor provide, albeit at lower spectral resolution, an independent and complimentary data set to TRs as MW frequencies can pass through non-precipitating clouds, over cloud covered regions where TRs are unable to at this stage. Studies demonstrated that assimilating MW radiances with variational DA algorithms improves forecasts in global NWP models over areas with few conventional observations (Simmons & Hollingsworth, 2002; Zapotocny et al., 2008) and in limited area NWP models when using variational data assimilation systems (Wang et al., 2021). Moreover, the simultaneous assimilation of TRs and MW satellite data provides the opportunity to compare the merits and challenges of assimilating one data set versus the other. In fact, while direct assimilation of satellite radiances in limited-area models can be rather laborious, TR assimilation into a limited-area model like WRF is straightforward from the user perspective. Direct radiance assimilation requires the use of a radiative transfer model, observation thinning, a good understanding of the limits and potentials of the sensors/channels involved, and, most of all, bias correction (Auligné, 2007; Auligné et al., 2007; Auligné & McNally, 2007; Dee, 2005). The latter can be cumbersome and challenging to implement, especially in limited-area models, due to the non-uniform coverage of polar orbiting satellites. In contrast, TRs' assimilation eliminates the need for a radiative transfer model. Once the NWP model is equipped with a dedicated assimilation module, minimal parameters tuning is needed, as most of the sensor-related parameters are handled by the retrieval processor (Mirto). While direct radiance assimilation of hyperspectral sensors with thousands of channels requires the understanding and tuning of many parameters, the retrieval process compresses all the underlying physical information into a very limited number of parameters (<20 eigenvectors), provides an ad hoc observation operator, and reduces the observation error covariance to the Identity Matrix regardless of the hyperspectral sensor's characteristics, thus limiting the amount of tuning needed by the users at assimilation time. The present study also shows that TR assimilation does not seem to require bias correction, as TR assimilation is ultimately more akin to single profile assimilation than radiance assimilation.

Three parallel experiments were designed to evaluate the impact of assimilating TRs and the combined assimilation of TR and MW radiances in a WRF 3-hr cycling system on the system's nowcasting and forecasting accuracy. Each experiment produces analyses every 3 hr between 03:00 UTC 20 November and 12:00 UTC 18 December 2020. These analyses initialize 12-hr WRF forecasts. The Global Forecasting System (GFS) and European Centre for Medium-Range Weather Forecasts (ECMWF) analyses, available at synoptic times, are used to validate the WRF predictions.

This paper is structured as follows: Section 2 provides the working framework in terms of the description of the involved models' configurations and the observational data availability; Section 3 describes the experiments design and Section 4 the adopted validation strategies; and results are presented in Section 5. Conclusions and future work are outlined in Section 6. This work was conducted at the Mauna Kea Weather Center (MKWC) in Hawaii. The MKWC is a weather research and forecast facility funded by the astronomical observatories on Mauna Kea (Businger et al., 2002; Cherubini et al., 2011, 2021; Lyman et al., 2020; http://mkwc.ifa.hawaii.edu), and routinely runs the WRF Model system.

Table 1
Weather Research and Forecasting Configuration

Domain parameters			
E-W *n* of grid points	N-S *n* of grid points	$\Delta x = \Delta y$ (km)	Integration time step
451	451	4,500	30 s
Map projection	Mercator		
Physical packages			
Microphysics	WRF single-moment 6-class microphysics scheme which allows for ice, snow, and graupel (Hong & Lim, 2006)		
Cumulus	Tiedtke cumulus convention scheme (Zhang & Wang, 2017)		
PBL	Mellor-Yamada-Janjic (MYJ) planetary boundary layer scheme (Janjic, 2002)		
Radiation	RRTM longwave-shortwave radiation scheme (Dudhia, 1989; Mlawer et al., 1997)		
Land surface	Noah land surface model (https://ral.ucar.edu/solutions/products/noah-multiparameterization-land-surface-model-noah-mp-lsm)		
Surface Layer	Eta similarity surface layer scheme (as used in Eta Model)		

2. Model Set Up and Data Availability

The underlying working framework used in this study is partially described in Section 2 of A2020. The chosen WRF model configuration encompasses the domain in Figure 1 of A2020, with horizontal grids spacing of 4,500 m centered over the north-central Pacific area and the island of Hawai'i, which correspond to the coarser and parent domain in the MKWC operational configuration (A2020 and Table 1). A custom adaptation of the WRF Data Assimilation system version 3.9.1, which includes modules to assimilate TR, is used in this study (Antonelli et al., 2015, 2020; DeHaan et al., 2015). The WRFDA is capable of ingesting a wide variety of observation types. The different data sets used in the assimilation experiments in this study are described hereafter.

2.1. Conventional Observations

In data assimilation experiments, in situ observations are the classical and most commonly used type of data. They include conventional radiosondes as well as ground and upper air observations. Only two radiosondes are available in the Central Pacific Area: Hilo (PHTO, 91285) and Lihue (PHLI, 91165) radiosondes. Other conventional observations include: METAR, SYNOP, ship and buoy for ground observations; and TEMP, AIREP, ACARS, TAMDAR for upper air observations. The WRFDA is also capable of assimilating some remote sensing derived products. Among these, Atmospheric Motion Vectors (AMV, Cherubini et al., 2006) and QuickScat winds are present in the data used in this study. For the sake of simplicity, we refer to them as "Conventional Observations" (CO) throughout this paper (National Centers for Environmental Prediction et al., 2008). This data set is the output from the final step of the NCEP GFS Data Assimilation System (GDAS), which prepares the majority of conventional observational data for assimilation into various NCEP analyses. A certain level of quality control (QC) is already performed to this data set before making it available. WRFDA is capable of ingesting these data "as is" with no pre-processing necessary (https://www2.mmm.ucar.edu/wrf/users/wrfda/Docs/user_guide_V3.9.1/users_guide_chap6.htm#_Running_Observation_Preprocessor_2). Figure 1 shows examples of the typical geographical distribution of available conventional observations.

2.2. Transformed Retrievals

Level 1 data from both the CrIS and IASI sensors on *Suomi NPP* and *NOAA-20*, and *MetOp-A/B/C* for the period from 20 November to 31 December 2020 were fed to the Mirto processor (A2017), which produced 1DVAR physical retrievals of temperature and relative humidity (RH), instability indices, and TRs, along with their observation operators for the entire timeframe. The TRs and their corresponding observation operators are the quantities used in the assimilation process within the modified WRFDA system (A2020). Although the version of Mirto under development is capable of retrieving information on cloudy-sky conditions also, only retrievals in clear-sky conditions are included in this study. The generation of TRs above cloud top and the impact of assimilating them is left for future investigations.

An example of the distribution of clear-sky fields of view (FOVs) associated with successful Mirto retrievals is provided in Figure 2. This distribution is obtained by patching together the CrIS data from adjacent *Suomi-NPP* overpasses that overlap the model domain and occur during the 2-hr windows centered at 12:00 UTC on 1 December 2020. The aggregated data for each overpass are quality controlled and then thinned to 80 km. The performed QC is described in A2020.

The TRs are assimilated in WRFDA by an adapted version of the original satellite radiance module (A2020, Section 3b). The TR observation operators are characterized by at most 20 eigenvectors of the Signal to Noise matrix (Migliorini, 2012; Migliorini et al., 2008). In the current WRFDA implementation only eigenvectors associated with eigenvalues of the signal to noise matrix greater than 1 are retained. Due to refinements of the a-priori covariance matrix in Mirto, 15 of the available 20 eigenvalues are actively assimilated (vs. 12 over 20 of the previous study). The TRs used in the experiment timeframe consistently show that the bulk of the

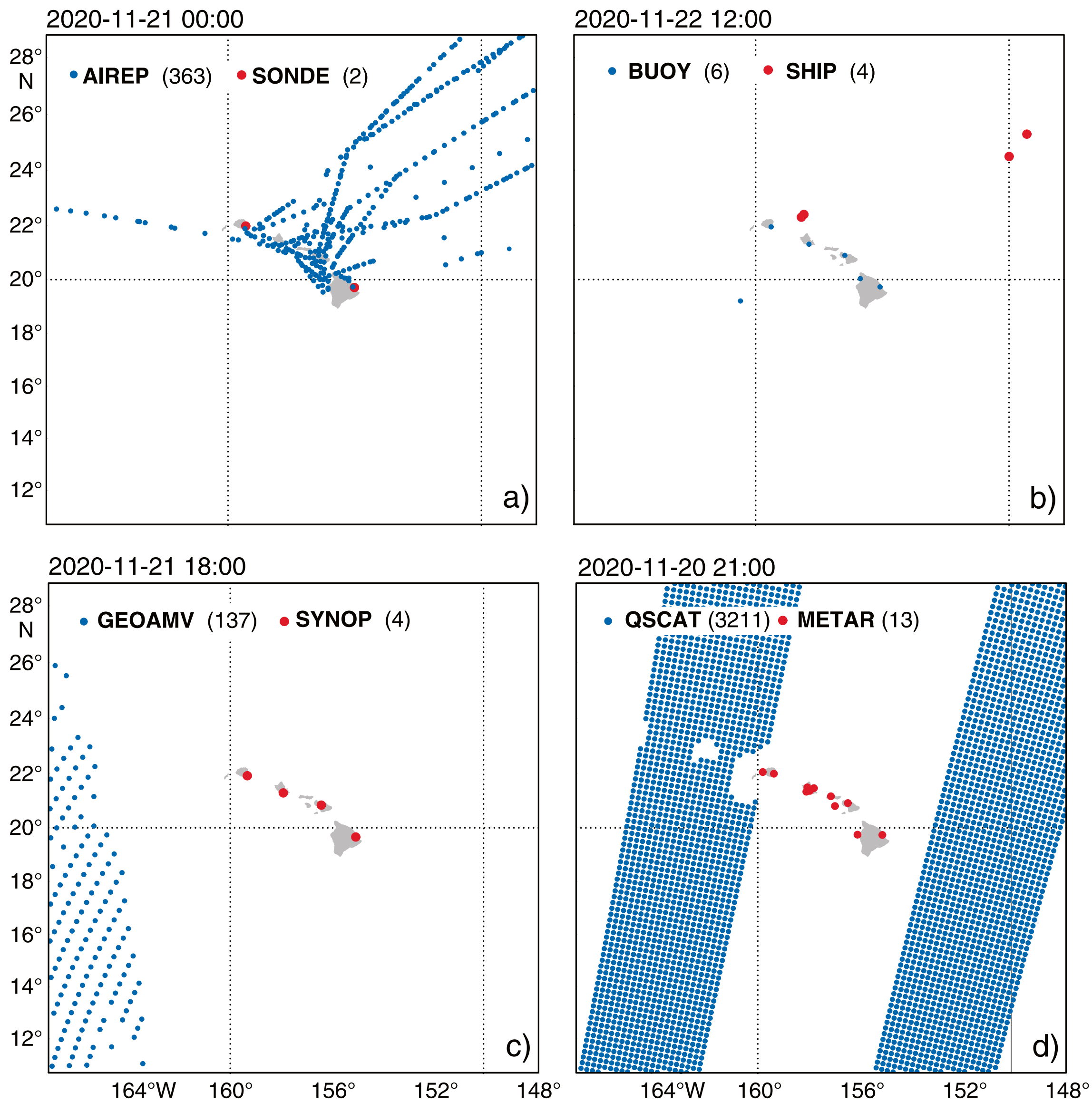

Figure 1. Examples of the spatial distribution of conventional observations available from the Global Data Assimilation System. (a) Aircraft Report (AIREP) data (blue) and radiosonde launching sites (red); (b) Buoy (blue) and ship (red) report data; (c) Geostationary Atmospheric Motion Vectors and Surface Synoptic Observations (SYNOP) data; and (d) QuickScat data and METeorological Aerodrome Reports (METARs). The spatial distribution of each individual data set and amount of data (indicated in parenthesis) varies with time.

information from the underlying hyperspectral sensors is carried by, at least, the first 15 eigenvectors (Figure 3). Within WRFDA, eigenvector selection for TR works just like channel selection for radiance assimilation (https://www2.mmm.ucar.edu/wrf/users/wrfda/Docs/radiance_userguide_v1.pdf, page 6). A QC is implemented within the assimilation module that rejects any normalized observation whose difference with the background is outside the 3-σ confidence interval (A2020). In the current configuration of Mirto and the WRFDA module for TR assimilation no bias correction scheme has been implemented. Although bias correction is very relevant for radiance assimilation experiments to be successful (Eyre, 2016), our results seem to suggest that there is no need for bias correction in TR assimilation (see Section 3).

2.3. MicroWave Radiances

The microwave radiances used are from: (a) Advanced Microwave Sounding Units A (AMSU-A) on board of various satellite systems (Aqua, METOP-A/B, NOAA18/19), which has 15 channels in the microwave range; (b)

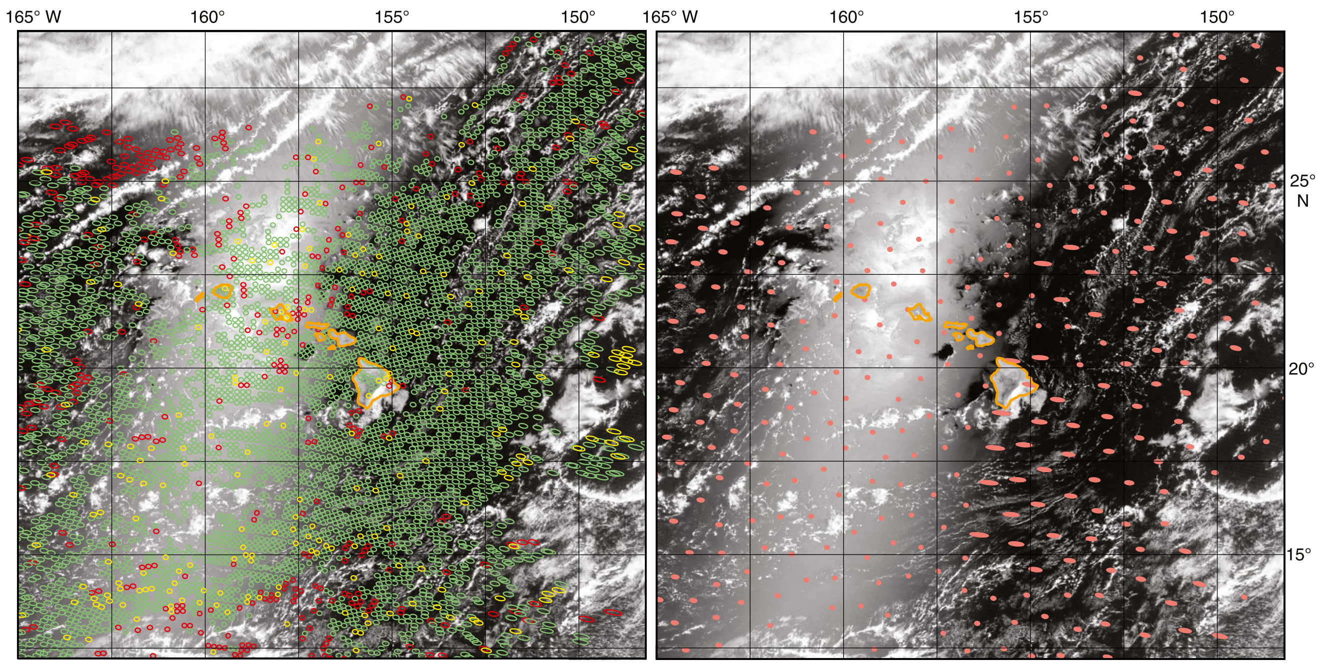

Figure 2. Locations of convergent, non-saturated CrIS retrievals (relative humidity < 100% for any level) obtained from two adjacent *Suomi-NPP* overpasses, (a) before and (b) after the 80 km thinning is applied. Data are overlaid on a VIIRS true color image valid for 00:00 UTC 01 December.

Microwave Humidity Sounder (MHS), which has five channels in the MW range, on board the NOAA-18/19 and METOP-A/B; and (c) Advanced Technology Microwave Sounder (ATMS), which currently flies on the *Suomi NPP* and NOAA-20 satellite missions and senses the atmosphere through 22 channels. These sensors, which observe the Earth in the MW portion of the electromagnetic spectrum, can "see" through clouds. Although available, the *MetOP-C* MW radiance data are not used in this study because their assimilation capability is only implemented from WRFDA version 4.3. Table 2 summarizes the sensors included in the assimilation and also indicates which channels are actively assimilated. Only channels active in the default set up of the WRFDA are used here. Sensitivity tests for the number of channels used is beyond the scope of this study (www.emc.ncep.noaa.gov/mmb/data_processing/Satellite_Historical_Documentation.htm). IASI and CrIS radiance data are not included in this experiment to avoid the same information content being assimilated twice. However, IASI and CrIS radiance data could be present in the initial conditions of the cold-start cycles because the GFS fields are the results of the NCEP GDAS, which assimilates radiances from these sensors. Moreover, only radiance data in the MW range is included, as it is believed to provide information complementary to that from hyperspectral sensors.

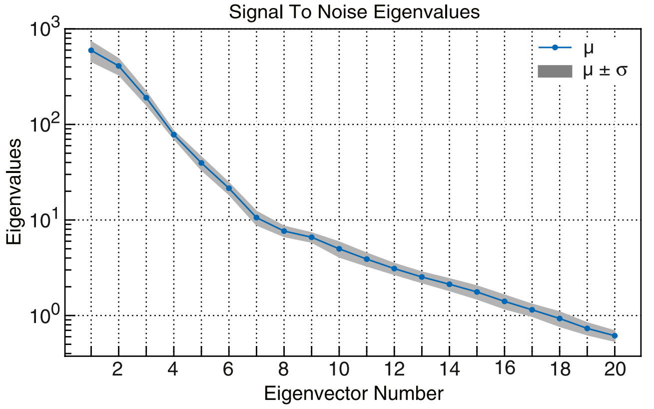

Figure 3. Logarithmic distribution of eigenvalues (mean and standard deviation) of the signal-to-noise matrix (Equation 7 in A2020) for 01 December 2020 at 12:00 UTC. Three hundred thirty-three IASI fields of view (FOVs) with 3,306 channels per FOV were assimilated. The eigenvalues larger than 1, are those that actually carry significant information about the true state vector. For this particular scenario 17 eigenvectors are >1.

3. Experiment Set Up

The WRF modeling system can run in cold-start mode, which uses the NCEP GFS analyses and forecast as initial and boundary conditions, or in cycling/hot-start mode, where each forecast cycle is initialized using the forecast from the previous cycle as background, and a custom analysis is created by ingesting available local observations in WRFDA. A 3-hr cycling frequency is used and the WRF forecasting system is refreshed with a cold-start run every 3 days. Whether in cold-start or cycling mode, each forecast is 12-hr-long for the purpose of this study (Figure 4). Each forecast is kept short to limit the amount of output data given the long experiment timeframe. Moreover, at this stage, the focus is on the analyses and early simulation hours, which are the ones likely to carry the largest effect from the assimilation process as described in A2020.

Table 2
Assimilated MicroWave Radiances: Microwave Humidity Sounder (MHS) Channels Probe the Water Vapor Absorption Lines, AMSUA the Oxygen Absorption Lines, While Advanced Technology Microwave Sounder Sense (ATMS) a Larger Swath of the Spectrum Containing Both Oxygen and Water Vapor Absorption Lines

Satellite ID	Sensor	Channels	Frequencies (GHz)
NOAA-18/19	MHS	3,4,5	183.31
			183.31
			190.31
EOS-Aqua	AMSU-A	5,6,8,9	~(53.5–57.3)
NOAA-18/19	AMSU-A	5,6,7,8,9	~(53.5–57.3)
MetOP-A/B	AMSU-A	5,6,7,8,9	~(53.5–57.3)
MetOP-A/B	MHS	3,4,5	183.31
			183.311
			190.311
Suomi NPP	ATMS	6,7,8,9,10,18,19,20,21,22	~(53.5–183.31)

Three cycling assimilation experiments were configured. The first solely assimilates conventional observations and is hereafter referred to as the control (CO) experiment. The second experiment also assimilates the high-resolution infrared data in the form of TR and is hereafter referred to as the TR experiment. Finally, the third experiment also assimilates MW radiances and is hereafter referred to as FULL/TRMW experiment. Each experiment consists of a 3-hr cycling system that starts on 20 November at 00:00 UTC and ends on 18 December, at 12:00 UTC, 2020. Each experiment is cold-started every three days and comprises nine full cycles (nine cold start forecasts). Given the typical overpass times over Hawai'i of polar orbiting satellites carrying hyperspectral sensors, TRs are usually available for the 00:00/12:00 UTC (CrIS on *Suomi* NPP/*NOAA-20*) and 06:00–09:00/18:00–21:00 UTC (IASI on *MetOPs*) assimilation times. MicroWave radiances are available for the same times as the TRs are because *Suomi NPP/NOAA-20* carries both CrIS and ATMS, and *MetOP-A/B/C* carries both IASI as hyperspectral sensor and AMSU-A and MHS as MW sensors. Moreover, MW sensors are available on the NOAA constellation (NOAA-18/19) with AMSU-A. Figure 5 shows the geographical distributions of the TR and MW observations that were successfully assimilated from the sensors (IASI and AMSU-A) on board of *MetOP* and the sensors (CrIS and ATMS) on board JPSS. Aside from the difference in assimilated observations, the three experiments were otherwise configured identically. Only the observations within ±1 hr of the analysis time were assimilated and all observations were assumed to be valid at analysis time.

As for radiance assimilation, the Community Radiative Transfer Model (CRTM, Weng et al., 2005) is used and a Variational Bias Correction (VarBC, Auligné, 2007; Auligné & McNally, 2007; Auligné et al., 2007) applied. In particular, the VarBC is cold started (i.e., initial biases are unknown). On the first cycle of the sequence where radiance assimilation happens (20 November 2020 at 06:00 UTC) and VarBC bias predictor coefficients are updated throughout the experiment timeframe. A radiance data thinning of 80 km is applied during assimilation to avoid potential correlations between adjacent observations (Ochotta et al., 2005) and maintain consistency with the TR thinning. Figure 6 shows the effects of the applied VarBC to one of the ATMS channels for one of the assimilation times. A similar behavior is found for all used channels and times. On the other hand, Figure 7 seems to suggest that the TRs might not need a bias correction scheme and similar behavior is found for all assimilated eigenvectors. While VarBC is an important step in satellite radiance data assimilation, it can be challenging to perform, more so in limited area models, as it requires a deep understanding of the underlying predictors and anchoring observations (Auligné et al., 2007). VarBC also requires a spin up time in order to produce meaningful predictors (https://www2.mmm.ucar.edu/wrf/users/wrfda/Docs/radiance_userguide_v1.pdf, page 11).

As polar-orbiting satellite positions vary temporally, data from a given satellite may be unavailable over the computational domain at a particular analysis time. Given the typical overpass times of the satellite platforms

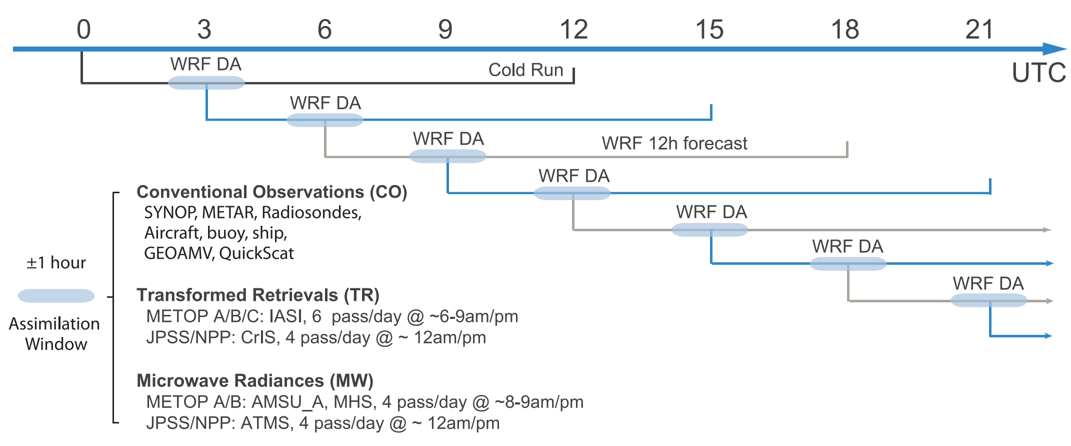

Figure 4. Weather Research and Forecasting cycling schedule and data flow.

10.1029/2022JD038153

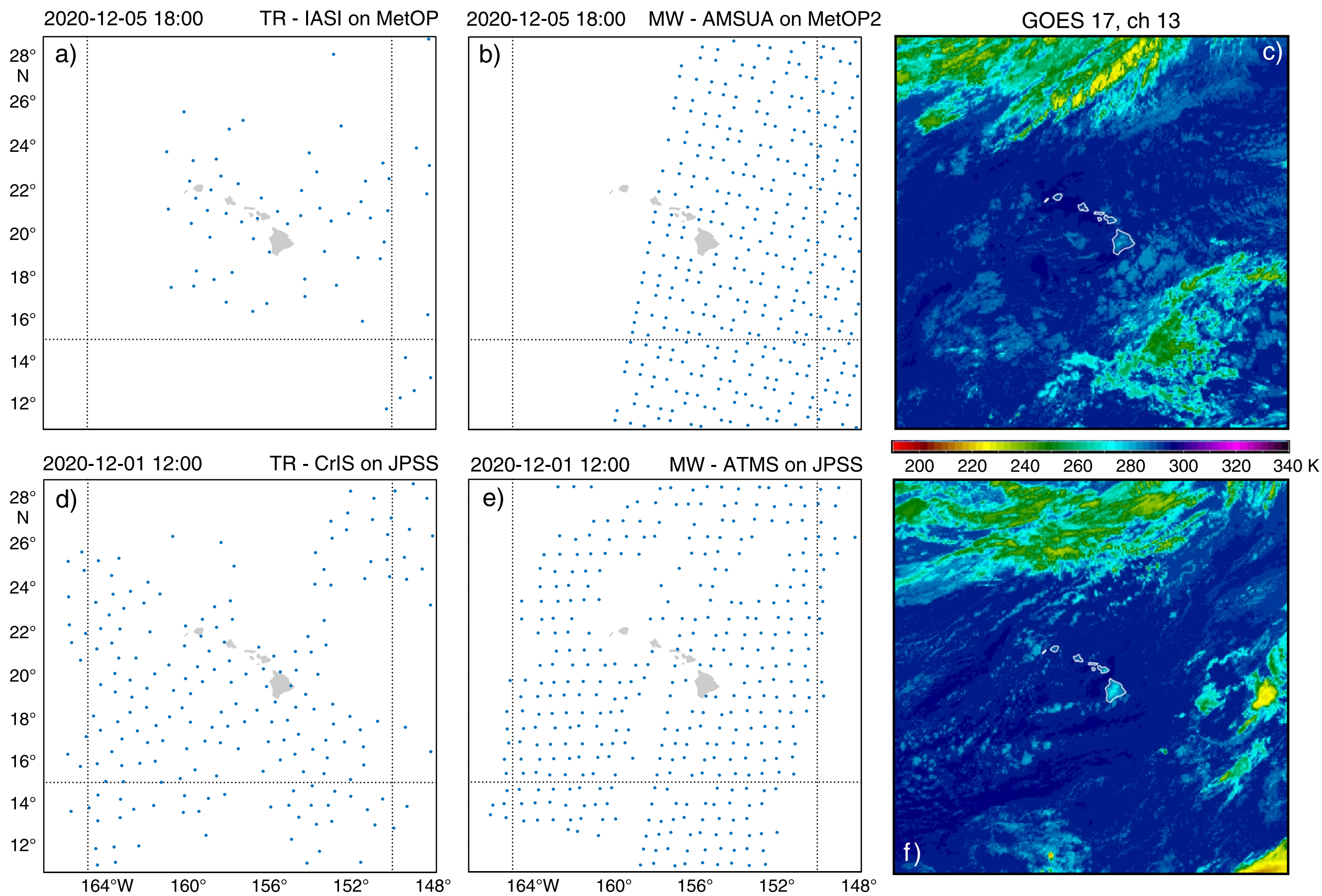

Figure 5. Fields of view (FOVs) locations on 05 December 2020 at 18:00 UTC0 UTC for (a) Transformed Retrieval (TR) from IASI on MetOP platforms and (b) MicroWave from Advanced Microwave Sounding Units A on MetOP-2 and (c) corresponding InfraRed GOES 17 image (channel 15, cloud top temperature); FOVs location on 1 December 2020 at 12:00 UTC0 UTC for (d) TR from CrIS on JPSS and (e) MW from Advanced Technology Microwave Sounder on JPSS and (f) corresponding Infra-Red GOES 17 image (channel 15, cloud top temperature).

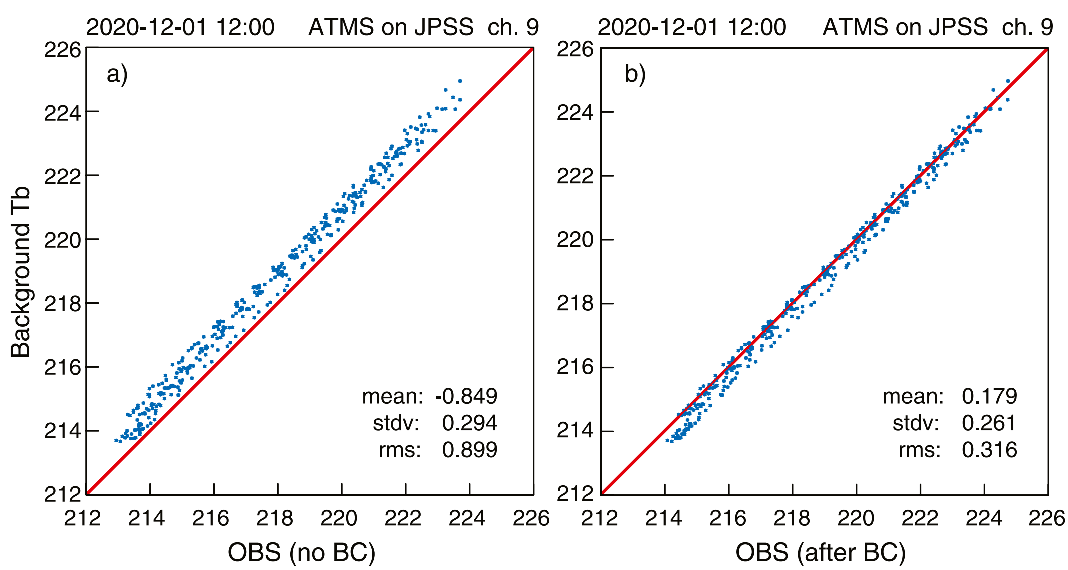

Figure 6. Scatterplots of observed versus computed brightness temperatures for JPSS Advanced Technology Microwave Sounder channel 9, (a) before and (b) after bias correction.

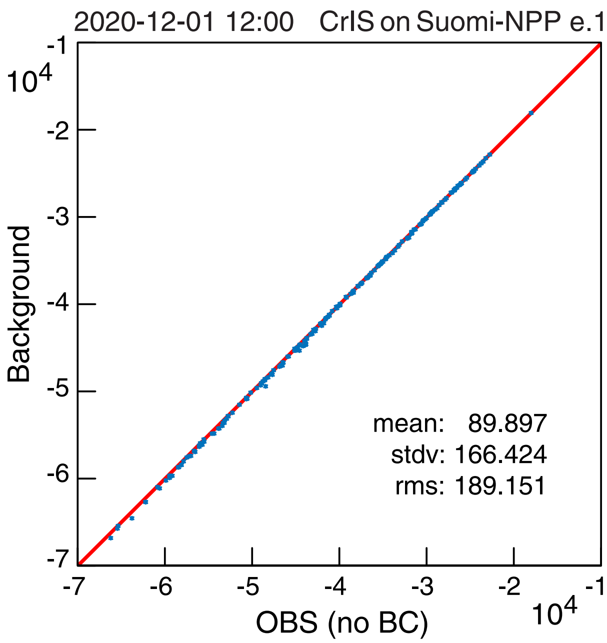

Figure 7. Scatterplot of observed versus computed Transformed Retrievals for Suomi NPP CrIS, corresponding to the first eigenvector. No BC is applied nor is one needed.

involved in this experiment, the cycling times with less or near nil satellite data availability are the 03:00 and 15:00 UTC (Figure 8). For the TR experiment the number of assimilated statistically independent data is (blue bar segments in Figure 7a):

$$N_{TR} = N_{TR\_FOVS} * N_{eigen} \tag{1}$$

where N_{TR_FOVS} is the number of assimilated TR FOVs and N_{eigen} is the number of assimilated eigenvectors that passed the internal/local quality check procedure. The number of assimilated eigenvectors can change during the various cycles depending on local conditions.

For the TRMW experiments the total number of assimilated data is (red bar segment in Figure 7a):

$$N_{TRMW} = N_{TR'} + N_{MW\_FOVS} * N_{MW\_ch} \tag{2}$$

where $N_{TR'}$ is the number of assimilated TRs data (which could differ from the case when only TR are assimilated, N_{TR}), N_{MW_FOVS} is the number of assimilated MW FOVs, and N_{MW_ch} is the number of actively assimilated MW channels. The amount of satellite data flowing into the TRMW experiment is broken down by sensor in Figure 7b, while Figure 7c shows the difference $\Delta N(TR) = N_{TR} - N_{TR'}$. In general, the number of TRs assimilated changes slightly through the various assimilation cycles depending on whether MW radiances are also assimilated. However, the difference is large on the first TR assimilation cycle. In fact, while the experiments start with a cold start forecast on 20 November 2020 at 00:00 UTC, only conventional observations and no satellite data of any kind are assimilated at the following cycle (03:00 UTC). At 06:00 UTC on 20 November 2020 the TRs, which are available for this time frame, are assimilated and not rejected by the WRFDA only in the experiment when MW data are also assimilated. A cycling system needs many observations in order not to diverge. Conventional observations might be too few and sparse in the region of interest, more so at asynoptic times, to realistically constraint a new cycle. The concurrent use of TR and MW seems to kick off the system sooner, highlighting the synergy and complementary nature of these two data sets.

The meteorological conditions during the experiment time frame included periods of fair weather, characterized by the effect of ridging and subsidence, alternating with frontal systems, and/or short-wave troughs, drifting through the modeled domain. The last week of November and the first week in December 2020 were particularly active with a series of troughs or short-wave troughs quickly passing through. A deeper marine boundary layer, with increased moisture and cloud cover characterized this period. In contrast, average weather conditions were rather benign during the timeframe from 08 to 15 December, with at most very weak and shallow fronts skimming across the northern portion of the model domain. A rather sharp upper-level trough impacted the area in mid-December (15–17), followed again by fair weather for the Christmas' holidays, and ahead of a short-wave trough that developed in a cut-off low over and east of the Big Island on the 27 and 28 of December. The role of the meteorological conditions on the results will be discussed in the results section.

4. Evaluation Methodology

Evaluation of the experiments performance is carried out in reference to two different analyses data sets: (a) the NCEP GFS analyses (NCEP 2015) and (b) the ECMWF Integrated Forecast System (IFS) CY41r2 High-Resolution Operational Analysis and Forecasts (ECMWF 2016). The GFS and ECMWF analyses are used to evaluate all the WRF forecast hours validating the synoptic times for which the global analyses are available. The ECMWF analyses, being the result of an independent model and different data assimilation system, provide complementary insights in the validation procedure. Moreover, the two global analysis data sets have different spatial resolutions. The GFS analyses are available at 0.25° resolution, which corresponds to ∼25 km horizontal resolution at the experiment latitudes. On the other hand, the operational ECMWF analyses, in which variables are originally available as spectral coefficients, are transformed at RDA to a regular 5120 longitude by 2560

10.1029/2022JD038153

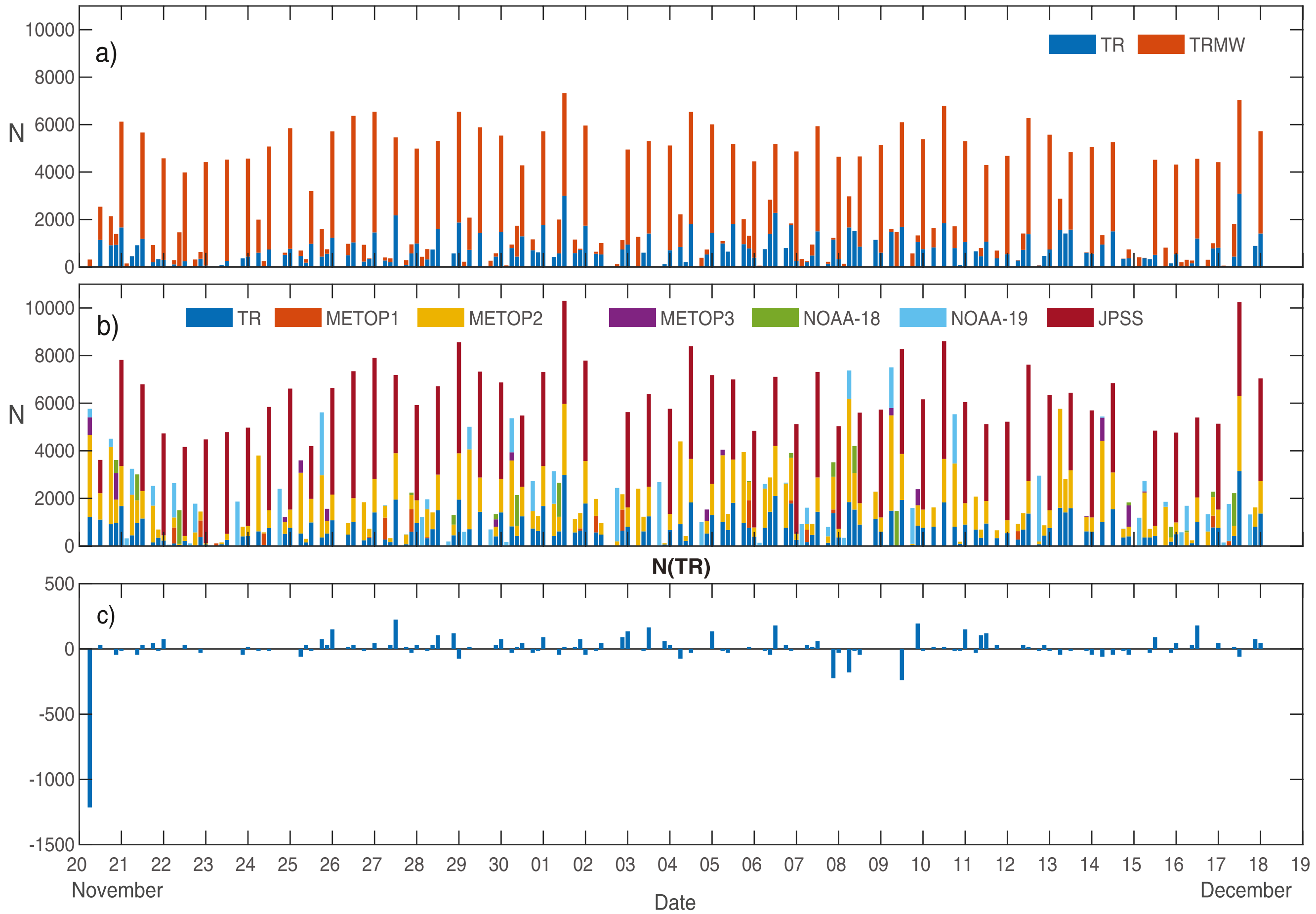

Figure 8. Number of satellite observations used at each assimilation cycle after passing quality control: (a) in the Transformed Retrieval (TR) (blue bar) and TRMW (red bar) experiments; (b) in the TRMW experiment broken down by sensor. (c) Difference between the amount of TR data assimilated in the TR experiment minus the amount of TR assimilated in the TRMW experiment.

latitude N1280 Gaussian grid, which results in an ~9 km (0.08°) horizontal resolution. Validation using analyses with different spatial resolutions provides insights on the model ability to reproduce processes on different spatial scales.

The WRF model outputs from each forecast cycle are interpolated from their original resolution (lat/lon regular, 4.5 × 4.5 km grid) onto both the GFS and ECMWF grids to allow for a comparison on a common scale. The WRF model output and global analyses are also interpolated on common pressure levels. Because WRF cycling frequency is 3 hr, and the global models' analyses are available at synoptic times only, the 6 and 12-hr WRF forecasts from the 00:00, 06:00, 12:00, and 18:00 UTC WRF cycles and the 3 and 9-hr forecast from the 03:00, 09:00, 15:00, and 21:00 UTC WRF cycles can be validated against global model analyses (Figure 9).

Statistics can then be built, aggregating the predicted variables of interest temporally and spatially over some or all the analyses time and on various levels. To objectively quantify the differences in the three experiments, the following statistical measures are used. The BIAS, RMSE, and bias corrected RMSE ($RMSE_b$) are defined as:

$$\mathrm{BIAS} = \sum_{i=1}^{N} \frac{F_i - O_i}{N} \tag{3}$$

$$\mathrm{RMSE} = \sqrt{\sum_{i=1}^{N} \frac{(F_i - O_i)^2}{N}} \tag{4}$$

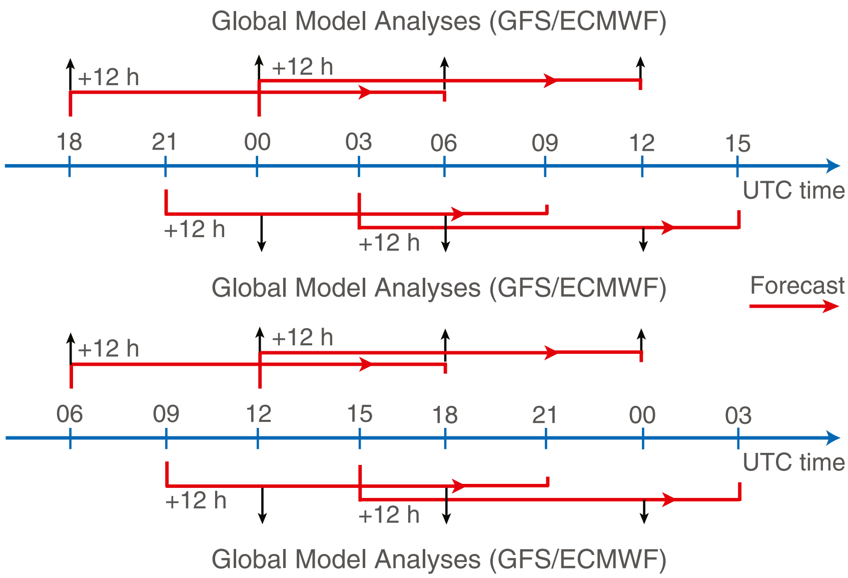

Figure 9. Verification strategy for 6- and 12-hr forecasts from 18:00, 00:00, 06:00, and 12:00 UTC cycles and 3- and 9-hr forecasts from the 21:00, 03:00, 09:00, and 15:00 UTC. The cycles can be validated against Global Forecasting System and European Centre for Medium-Range Weather Forecasts analyses.

$$\mathrm{RMSE_b} = \sqrt{\sum_{i=1}^{N} \frac{\left[(F_i - O_i) - \left(\overline{F_i - O_i}\right)\right]^2}{N}} \tag{5}$$

$$\Delta\mathrm{Err(TR)} = \frac{\mathrm{RMSE_b(TR.)} - \mathrm{RMSE(CO)}}{\mathrm{RMSE_b(CO)}} \tag{6}$$

$$\Delta\mathrm{Err(TRMW)} = \frac{\mathrm{RMSE_b(TRMW.)} - \mathrm{RMSE(CO)}}{\mathrm{RMSE_b(CO)}} \tag{7}$$

where, F and O refer to the forecast and observed field under investigation, respectively.

The ECMWF analyses at 00:00 and 12:00 UTC are the results of a sophisticated data assimilation system comprising more real time observations than those at 06:00 and 18:00 UTC (Haseler, 2004; Lean et al., 2020) and are, therefore, of higher quality than the 06:00 and 18:00 UTC analyses. For the sake of simplicity, only the 00:00 and 12:00 UTC analyses are considered when using ECMWF in this validation study.

Additional verification is performed against the radiosondes' data available from the two Hawaii locations (PHTO, Hilo; PHLI, Līhu'e). The $t_0 + 3$, $t_0 + 6$, $t_0 + 9$, and $t_0 + 12$ hr forecast vertical profiles for temperature, RH, and water vapor from the closest grid point to the two radiosondes' location are extracted and compared against the corresponding sonde's observations. Radiosonde soundings consist of a series of point measurements of atmospheric pressure, temperature, humidity, and wind at high resolution taken from a balloon borne instrument package as it ascends through the atmosphere. The advection of the ascending sonde by the wind results in the sonde drifting away from the launching location. The model vertical profiles instead represent the meteorological variables through the vertical column over the model grid point closest to the radiosonde location. To allow for a fairer comparison, the radiosonde profiles are interpolated on the model vertical grid. This validation does not include the model analysis time (t_0) as radiosondes are also included in the CO assimilation and, therefore, are not an independent set of observations for this particular time.

The main statistical measure used is the bias corrected RMS (Equation 5). For validation against global model analyses, the results are stratified by forecast hour and averaged throughout all the forecast cycles (00:00, 03:00 UTC… etc.).

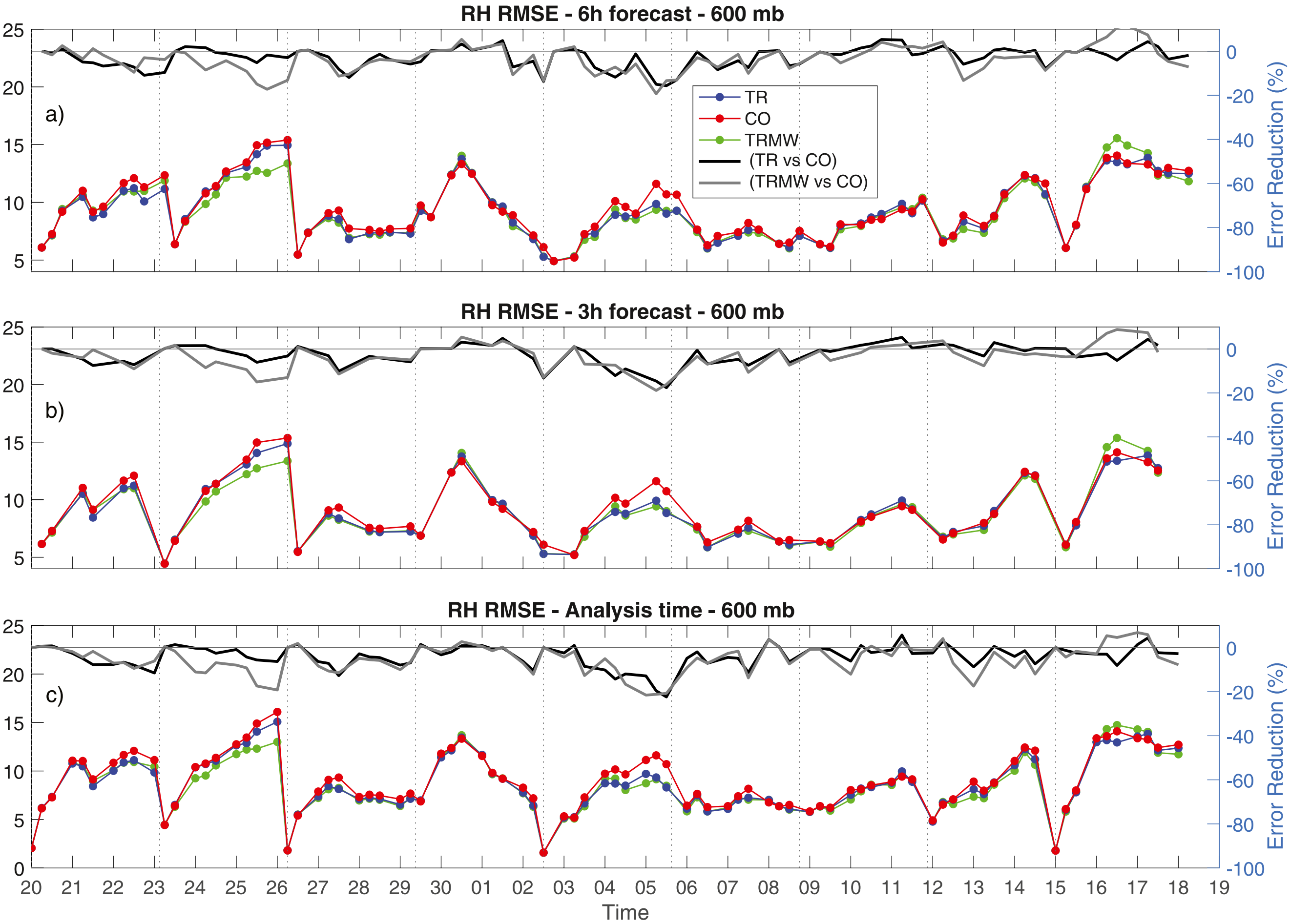

Figure 10. The $RMSE_b$ of the (a) 6, (b) 3 hr forecast relative humidity, and at analysis time (c) at 600 mb, over a 1 month period. Graphs show CO (red line), Transformed Retrieval (TR), (blue line), and FULL, TRMW (green line) experiments. Also included are the graphs for the error reduction (right axes) in percent for the TR versus the CO runs (black line) and the TRMW versus the CO runs (gray line). Global Forecasting System analyses are used as reference field in the statistics.

5. Results

Most of the results discussed hereafter refer to the effect of satellite assimilation on the moisture field RH. In fact, the assimilation of TRs has a greater impact on the characterization of the water vapor distribution than the temperature field because of the higher spatial variability of the water vapor concentrations and independence of the water vapor field from temperature and pressure (A2020).

The RH bias corrected RMSE (RH $RMSE_b$, Equation 5) time series for each of the three month-long experiments are calculated considering the RH WRF forecasts at the validating time and chosen level (600 and 800 hPa), and the corresponding RH GFS analyses (Figures 10 and 11). The grid points falling on land are excluded from the calculations because of the relatively coarse resolution of the global model when compared to island dimensions and complex topography. The statistics are averaged over the WRF domain and stratified by validation date and time. The time series highlight the consecutive cycling experiments: a cycle is the results of eight WRF simulations, each providing a 12 hr long forecast. The statistics show decreasing absolute forecast accuracy with an increasing cycling number (i.e., away from each cold start) within the same cycle, but an increasing relative accuracy (lower $RMSE_b$) for both the TR and TRMW experiments compared to the control run where only conventional observations are ingested. As expected, the improvement in the forecast accuracy performance is cumulative through each 3-day model cycle and accentuated even more on the 800 hPa level (Figure 11). It is also consistent throughout most of the month-long timeframe, although there are periods when the differences between experiments are quite small (assimilation cycles 4, 7, and 8). These periods correspond to spells of relatively calm weather in the area of interest and, therefore, the additional assimilated data might not add much more

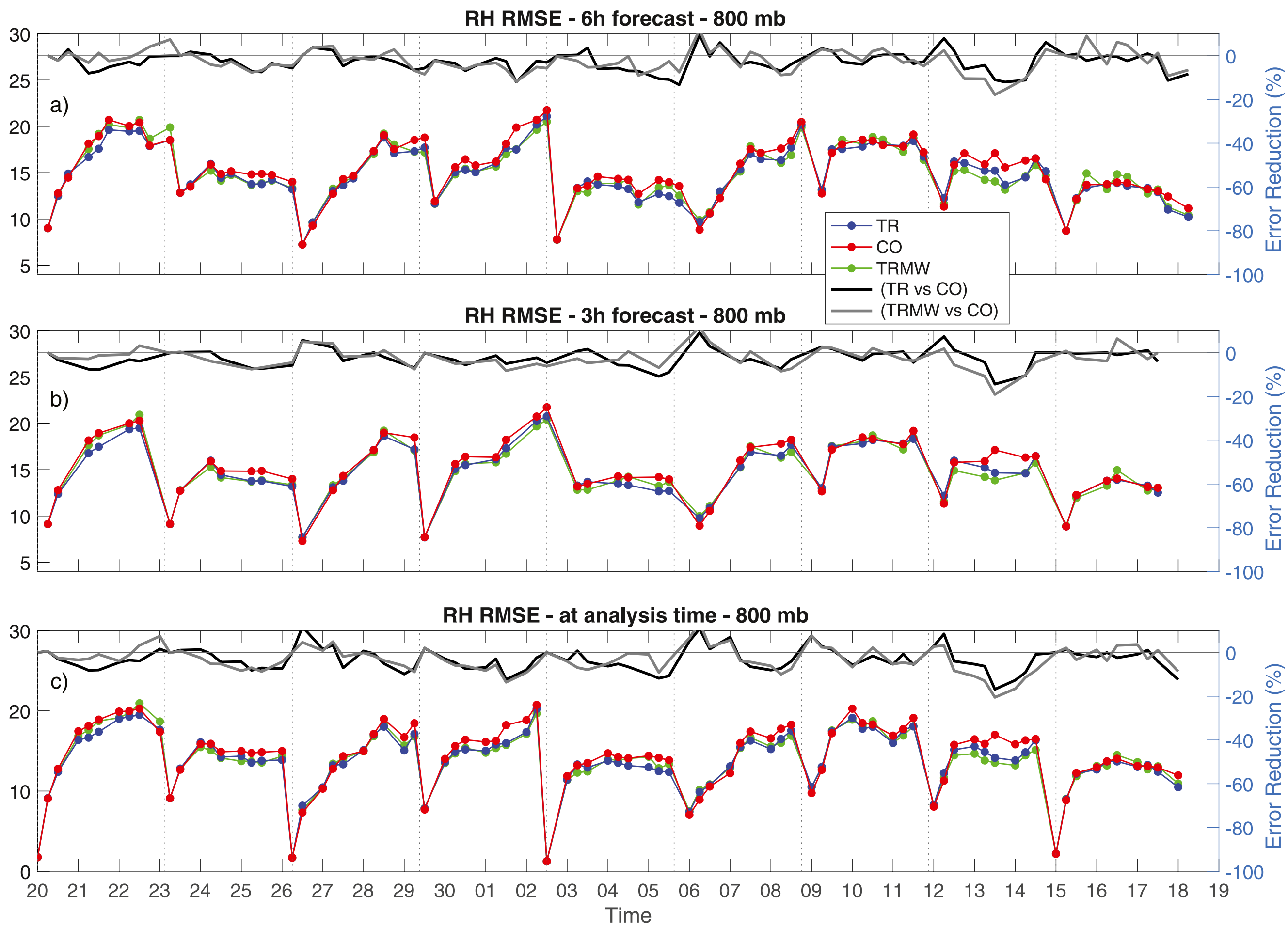

Figure 11. $RMSE_b$ of the (a) 6, (b) 3 hr forecast relative humidity and at analysis time (c) at 800 mb, over a month: CO (red line), Transformed Retrieval (TR), (blue line), and FULL, TRMW (green line) experiments are shown. Also included are the graphs for the error reduction (right axes) in percent for the TR versus the CO runs (black line) and the TRMW versus the CO runs (gray line). Global Forecasting System analyses are used as reference field in the statistics.

information into the custom analyses. The error reduction when assimilating TR, or TR and MW beside CO can reach values of 15%–20% by the end of each full assimilation (24 cycles).

In the second assimilation cycle (23–26 November), the TRMW experiment performs better than the control and the TR experiment, at the 600 hPa level. In all the other cycles where TR outperforms the control run, the TRMW experiment either performs equally or slightly worse. Both the 3- and 6-hr forecasts show a similar impact.

These results can be explained by the underlying amount of information provided by the TRs, which are a compressed form of information from thousands of hyperspectral sensor channels. In contrast, MWs, although available in larger numbers in terms of FOVs, have fewer channels (~tens or less) and are correlated within a single FOV due to their broad and overlapping weighting functions. On the other hand, the TRs provided by Mirto are uncorrelated quantities from thousands of correlated channels. When the ECMWF is used as true state in the $RMSE_b$ calculation in Equation 5, the RH $RMSE_b$ time series for the 600 hPa level (Figure 12) shows very similar results to those obtained when GFS is used in the validation. On the other hand, a larger improvement is found on the 800 hPa level (Figure 13) when TR are assimilated, both with and without MW. This finding is true for all analyzed forecast hours 0, 3, and 6. This particular result is encouraging for several reasons.

The improvement at 800 hPa is likely due to a refinement in the vertical definition of the trade wind inversion. An increased model performance against higher resolution analyses (ECMWF) points to better custom WRDA analyses. Smaller scale moisture structures that would usually be smoothed out by the coarser GFS analyses resolution are captured instead. The custom analysis from the assimilation of TRs improves with respect to an

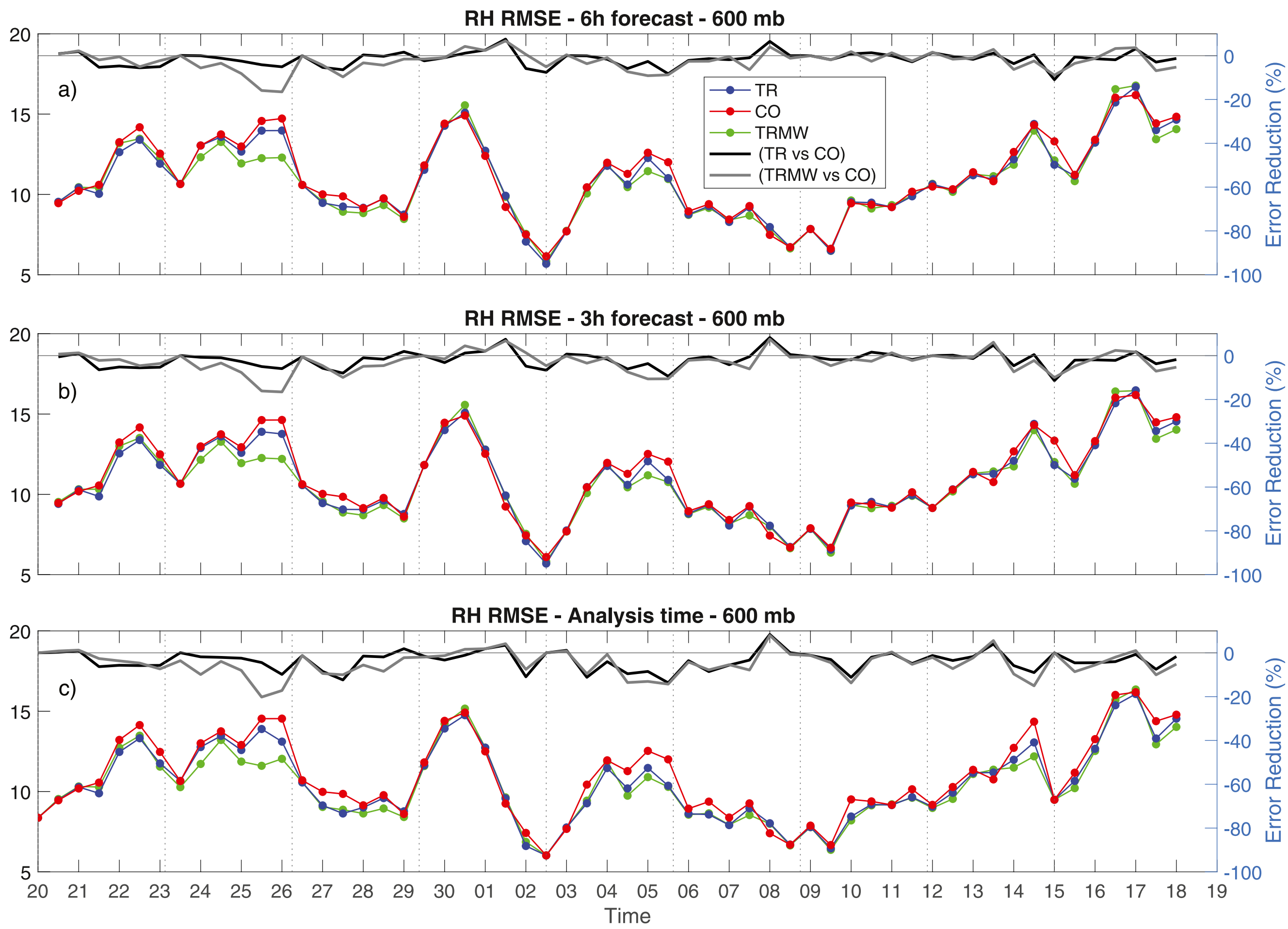

Figure 12. $RMSE_b$ of the (a) 6, (b) 3 hr forecast relative humidity and at analysis time (c) at 600 mb, over a 1 month period. Graphs show CO (red line), Transformed Retrieval (TR), (blue line), and FULL, TRMW (green line) experiments. Also included are the graphs for the error reduction (right axes) in percent for the TR versus the CO runs (black line) and the TRMW versus the CO runs (gray line). European Centre for Medium-Range Weather Forecasts analyses are used as reference field in the statistics.

independent and higher resolution analysis provided by ECMWF. On the other hand, validating against ECMWF analyses versus GFS analyses shows similar gains in the middle/higher levels of the atmosphere as meteorological fields are naturally smoother in the free atmosphere, being further removed from the effects of turbulence induced by surface friction.

5.1. Impact of Assimilation on Vertical Profiles

Vertical profiles of $RMSE_b$, for temperature and RH, averaged throughout the model domain, are also analyzed (Figures 14 and 15). Given all the possible statistical stratifications (e.g., variable, analysis type, forecast hour, and cycling time) it would be too lengthy to show and discuss all of them here. Both the TR and TRMW experiment show an increase in the 3 hr forecast accuracy in the moisture field between 900 and 300 hPa when the GFS is used as the reference field (Figure 14b). On the other hand, the impact of assimilating both sources of data on the temperature field is very small (Figure 14a). Figure 15 shows the same but when ECMWF analysis is used as the reference field and the results are similar. Very similar results are also found for all the analyzed profiles/cases: the assimilation of TR alone and both TR and MW improves the 3, 6, and 12 hr forecast accuracy in the middle atmosphere, from about 850 to 300 hPa. Also, the larger impact of the TR assimilation is found in the lower portion of this range, in the atmospheric layer from 700 to 600 hPa. Figure 16 shows three more cases during the time from 25 November at 18:00 UTC to 26 November at 06:00 UTC. This time period corresponds to the end of the second assimilation cycle. Again, the largest impact from TR assimilation is found in the lower portion

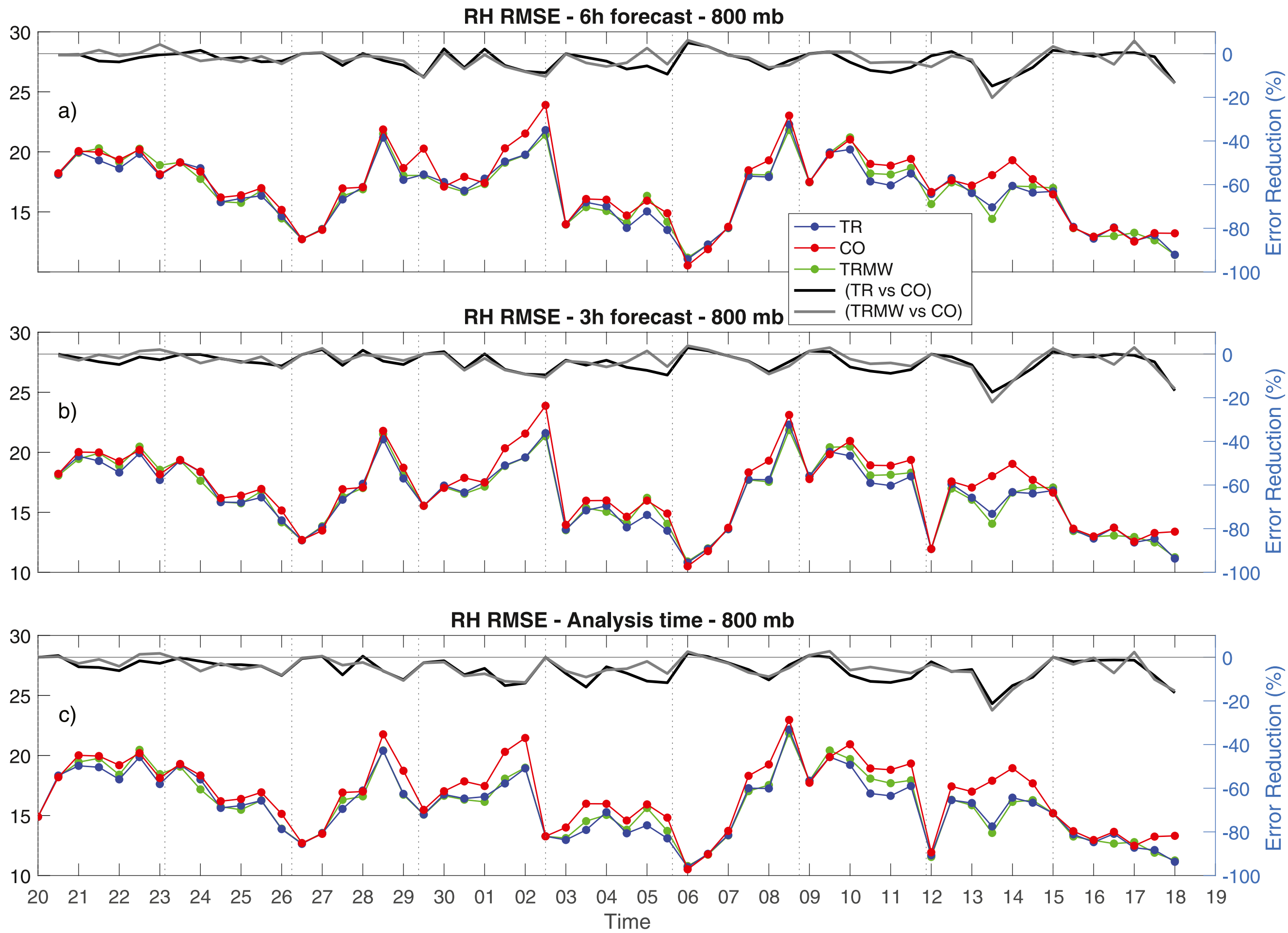

Figure 13. RMSE$_b$ of the (a) 6, (b) 3 hr forecast relative humidity and at analysis time (c) at 800 mb, over a 1 month period. Graphs show CO (red line), Transformed Retrieval (TR), (blue line), and FULL, TRMW (green line) experiments. Also included are the graphs for the error reduction (right axes) in percent for the TR versus the CO runs (black line) and the TRMW versus the CO runs (gray line). European Centre for Medium-Range Weather Forecasts analyses are used as reference field in the statistics.

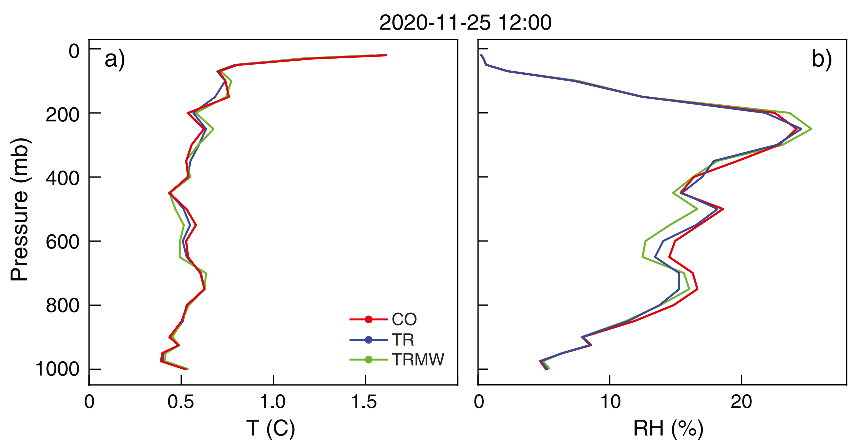

Figure 14. Vertical profiles of RMSE$_b$ for the 3 hr forecast temperature (a) and relative humidity (b) on 25 November 2020 at 12:00 UTC for the CO experiment (red line), Transformed Retrieval experiment (blue line), and TRMW experiment (green line). The Global Forecasting System is used as reference field in the statistics.

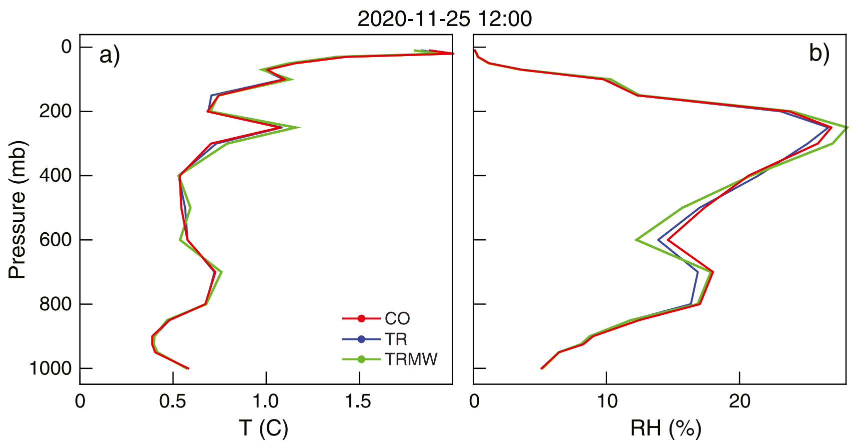

Figure 15. Vertical profiles of $RMSE_b$ for the 3 hr forecast temperature (a) and relative humidity (b) on 25 November 2020 at 12:00 UTC for the CO experiment (red line), Transformed Retrieval experiment (blue line), and TRMW experiment (green line). The European Centre for Medium-Range Weather Forecasts is used as reference field in the statistics.

of the middle atmospheric layers. On the other hand, MW assimilation has a large impact in the 600 to 300 mb, complementing TRs at these levels. TR availability during this cycle is low (Figure 8) in comparison to the rest of the timeframe, likely due to increased cloud coverage. Figure 16 also shows the error reduction when TR (Equation 6) and TRMW are assimilated (Equation 7) besides CO as a function of the pressure levels. Consistently, it shows that the assimilation of TR improves the model performance in the 900 to 700 mb range, while MW assimilation along with TR helps the model better perform in the 700 to 300 mb range. The TRs, underlying higher vertical resolution, better resolve the moisture around the tradewind inversion; on the other hand, the larger number of FOVs and broader MW weighting functions better capture the broader water vapor distribution in the middle tropospheric layers.

Validation against radiosondes observations is summarized in Figure 17 for the t_0 + 3hr and t_0 + 6hr forecasts. Results from this analysis are consistent with what was found in our validation against global model analyses: on average, both the TR and TRMW RH forecasts outperform the CO experiment in the middle atmosphere, from about 850 to about 350 hPa. Moreover, the TR experiment provides slightly better results at t_0 + 3hr than the TRMW experiment. Differences between experiments in terms of temperature $RMSE_b$ are generally quite small. However, while they seem negligible at t_0 + 6hr, small positive impact is found at t_0 + 3hr, particularly in the highest atmospheric levels (100–200 hPa) where a warm bias is often found in the model initial conditions when compared to observational data (Cucurull & Anthes, 2014). The error reduction in this layer is about 10% when assimilation of TR or TRMW is performed (not shown). The improvement from assimilating TR and TR and MW together is still discernible in the t_0 + 6hr RH forecasts.

5.2. Impact of Assimilation on Horizontal Synoptic Structures

The assimilation of TR alone and both TR and MW improves the 3-hr forecast accuracy on the 600 hPa level both when verifying against GFS (Figure 17) and ECMWF analyses (Figure 18). These figures, which includes all the 3-hr forecasts started at 09:00 UTC in the fifth assimilation cycle, shows how the areas of larger RMSEs shrank for the TR and TRMW experiments versus the control experiment. There is significant reduction everywhere, however, two areas stand out: (a) the area interested by the passage of a weak frontal system, north of the islands; (b) a large area in the Big Island's wake, in the southwestern quadrant of the model domain. The reduction of the former is perhaps an indication of a better handle by the forecast model of the location and timing of the frontal passage during those simulations. The area of greater errors in the wake of the Big Island is associated with the turbulent shifting of a convergence zone that results from the flow splitting around the high volcanos that make up the island. The higher errors are a reflection of sub-grid-scale processes that are not well captured by the global models but are captured by the higher resolution WRF model. Assimilation of TR alone or TR and MW results in a reduction of this forecast error. The smoother features in Figure 19 reflect ECMWF's higher resolution grid.

Figures 20 and 21 summarize these results when the entire experiment timeframe is considered. The RH $RMSE_b$ distribution for all the 3-hr forecasts started at 09:00 UTC in the month-long experiment and the 600 and 800 hPa

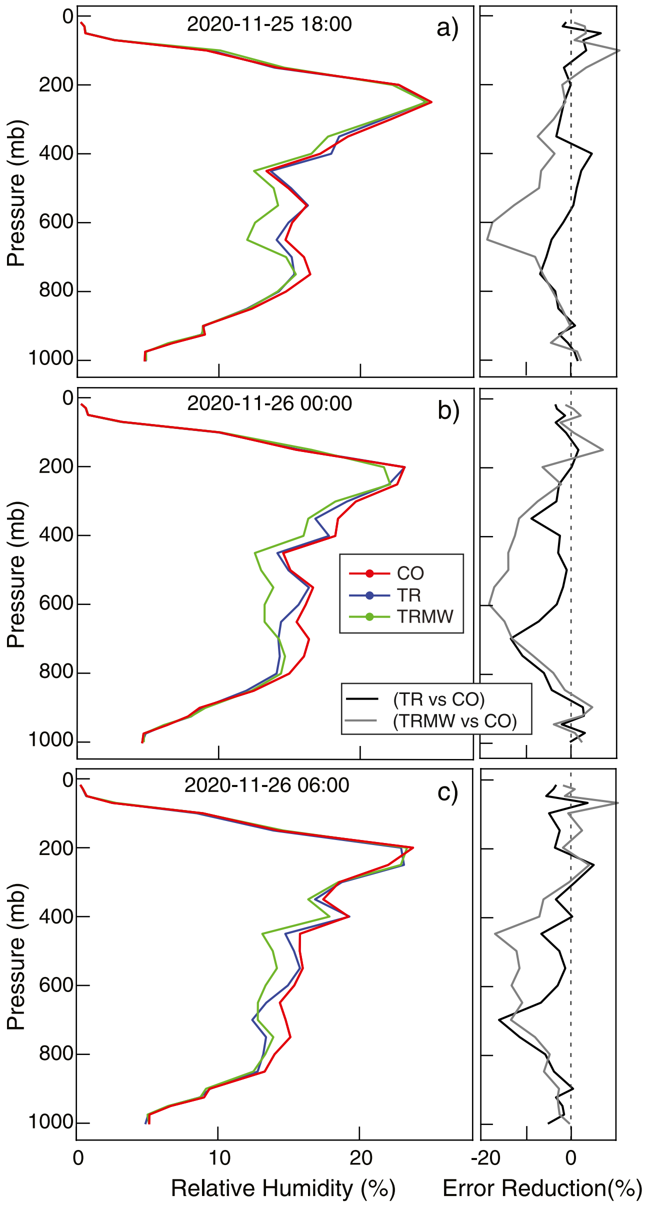

Figure 16. Vertical profiles of $RMSE_b$ for the: (a) 6 hr forecast started on 25 November at 12:00 UTC; (b) 3 hr forecast started on the 25 November at 21:00 UTC; and (c) 6 hr forecast started on 26 November at 00:00 UTC. The Global Forecasting System is used as the reference field in the statistics. The right subplot of each panel shows the error reduction when also Transformed Retrieval (TR) are assimilated versus when only CO are (black solid line) and when also TR and MicroWave jointly are assimilated versus when only CO are (gray solid line).

levels are shown using histograms. When both GFS and ECMWF analyses are used in the validation procedure, the distributions corresponding to forecasts where either TR or TR and MW were assimilated shift toward lower values, indicating a significant overall improvement in predicting RH in the middle atmospheric levels. The overall improvement is larger when ECMWF is used as reference field on the 800 hPa level (Figures 21c and 21d). This reinforces the conclusion made earlier those improvements at this level are larger due to better placement of the trade wind inversion.

6. Conclusions

This work is an extension of A2020 and presents the results of an assessment of the impact of TR assimilation into the WRF modeling system in a month-long experiment over the Central North Pacific Area. TRs are generated using the inversion system "Mirto" (A2017) while a modified version of the WRFDA model is used to ingest TRs. Three cycling assimilation experiments were configured: (a) control (CO) experiment, where only conventional observations are assimilated; (b) TR assimilation experiment, where high-resolution infrared data in the form of TR are also assimilated; (c) and a TRMW experiment, where MW radiances are also ingested. Each experiment consists of a 3-hr cycling system that starts on 20 November at 00:00 UTC and ends on 18 December, at 12:00 UTC, 2020. Each experiment is cold-started every three days and comprises nine full 3-day cycles. Each 3-day cycle contains 24 forecasts, initialized every three hours. For the purpose of this study, each forecast is 12-hr-long. Both the GFS and ECMWF analyses, available at synoptic times, were used to evaluate the impact of the new assimilation approach on the accuracy of the WRF forecasts. Radiosonde profiles available within the domain of interest are also used in the validation.

A comparison between model analyses and forecasts is performed on the horizontal and vertical grid each GCM analysis is defined on and the $RMSE_b$ is the main statistical measure used in the statistical analyses. For validation against radiosondes, observed profiles are interpolated on the model vertical grid over the model grid point closest to the sonde launching locations. Again, the $RMSE_b$ is used as main statistical measure.

This study confirms that assimilation of hyperspectral data has a larger impact on water vapor distribution than on the temperature field. The results of the statistical analysis can be summarized as follows.

- The positive results presented in this study seem to suggest that there is no need for Bias Correction. This implies that: (a) the a-priori information embedded in the retrievals is removed quite efficiently by the inversion process and (b) the hyperspectral radiances are radiometrically accurate.
- TR assimilation is ultimately more comparable to single profile assimilation than radiance assimilation.
- RH $RMSE_b$ timeseries on 800 and 600 hPa show a decreasing absolute forecast accuracy with the increasing cycling number, within the same 3-day cycle, but an increasing relative accuracy (lower $RMSE_b$) for both the TR and TRMW experiments compared to the control run where only conventional observations are ingested. The analysis of the error reductions, ΔErr(TR) and ΔErr(TRMW), quantifies the improvement in the 15%–20% range by the end of the 3-day model assimilation cycles.
- In most cycles, forecast accuracy after TR assimilation outperforms the control forecast accuracy. The forecast's accuracy after both TR and MW are assimilated either performs equally or slightly worse that

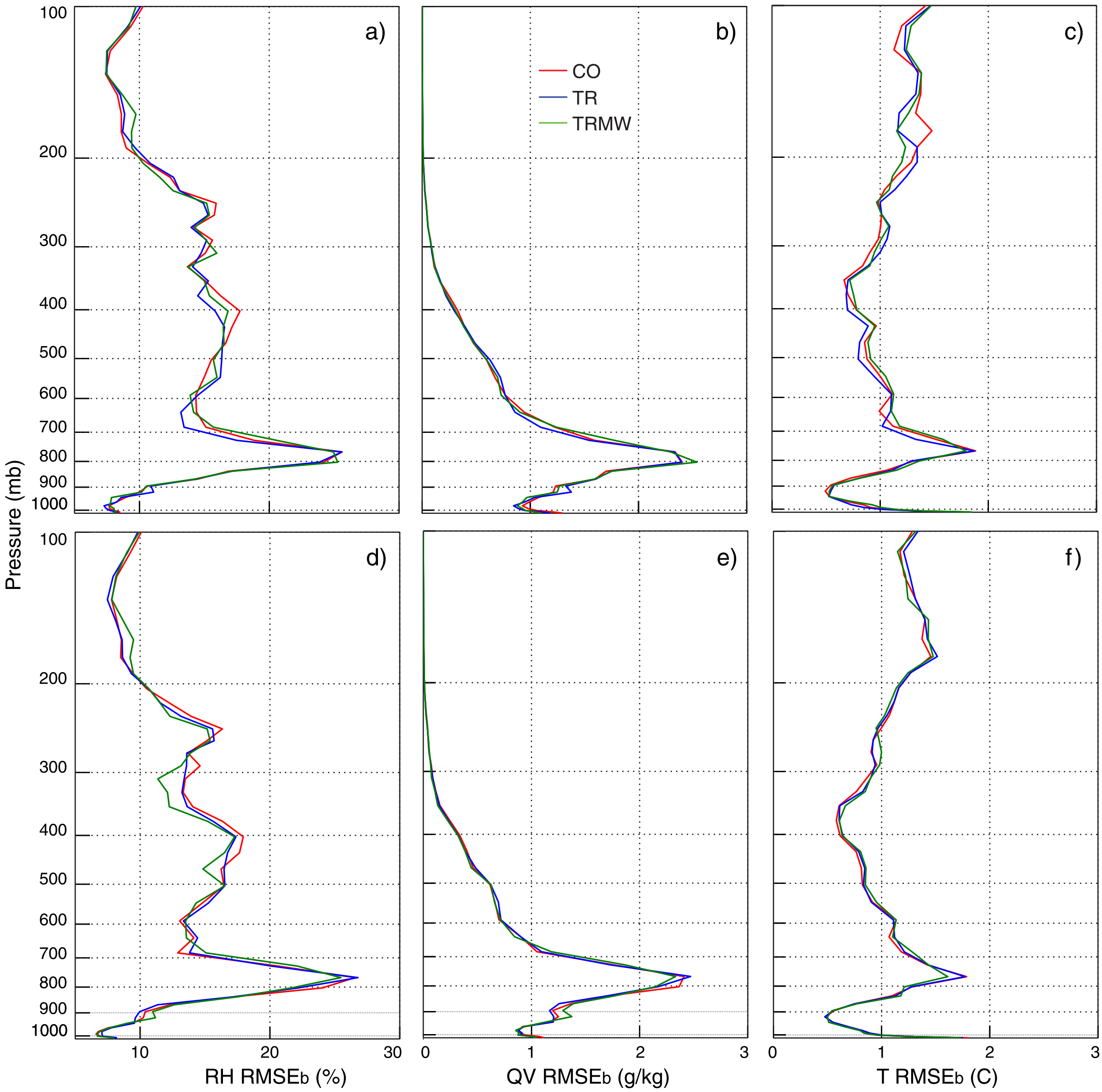

Figure 17. Vertical profiles of $RMSE_b$ for the (a) 3 hr relative humidity (RH), (b) Qv, and (c) T forecast, and (a) 6 hr RH, (b) Qv, and (c) T forecast throughout the entire experiment (20 November–20 December 2020). Radiosonde data are used as the reference field for model validation. The statistical sample comprises 107 forecasts. Cold start model runs are not included in the statistics.

assimilation only of TRs, but for one 3-day cycle (the second one in the sequence) when the number of available TRs was relatively small (due to higher cloud coverage).

- The improvement is even greater when ECMWF output is used as the reference field in the statistics particularly at the 800 mb level, for the shorter 3 hr forecasts, and at analysis time.
- The analysis of the RH $RMSE_b$ vertical profiles indicates that the assimilation of TR alone and combined assimilation of TR and MW improves the 3, 6, and 12 hr forecast accuracy in the middle atmosphere from about 850 to 300 hPa, both when the GFS and the ECMWF are used as reference field in the statistics. Also, a larger impact of the TR assimilation is found in the atmospheric layer from 800 to 600 hPa.
- The RH $RMSE_b$ cumulated over time and analyzed on the modeled domain at 800 and 600 hPa shows that forecasts after TRs assimilation perform better in predicting the timing and location of horizontal synoptic structures like fronts passing by. Also, the forecast's error is reduced in the convergence zone, which results from the flow splitting around the Big Island (Hawai'i). Moreover, the spatial RH $RMSE_b$ distribution

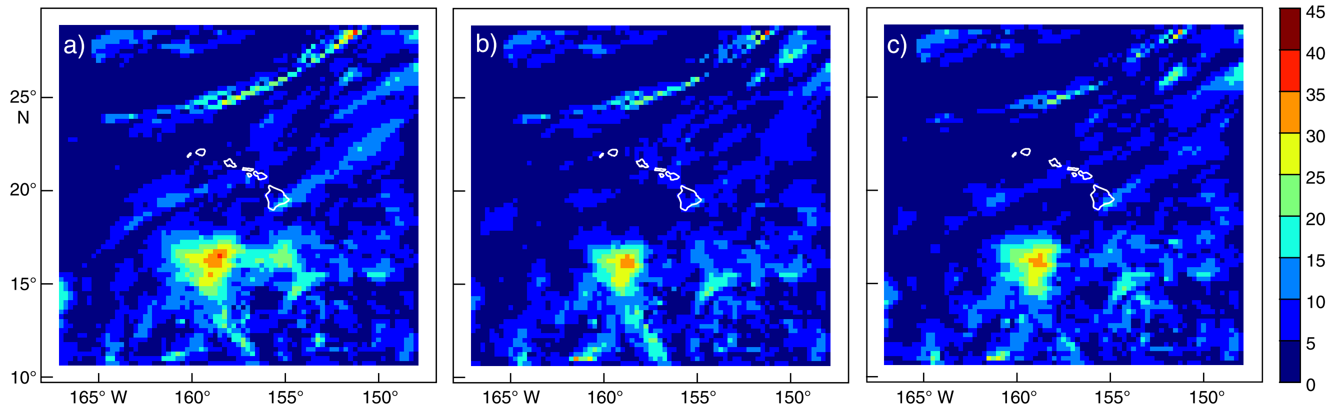

Figure 18. $RMSE_b$ for the 3 hr 600 mb relative humidity forecasts started at 09:00 UTC in the timeframe spanning from 02 December to 05 December (fifth cycle) when the Global Forecasting System is used as reference field in the statistics for experiment: (a) CO; (b) TR; and (c) TRMW.

calculated through the entire experiment timeframe shows significant improvement (lower $RMSE_b$) when TRs are assimilated both alone (best results) and in combination with MW. Results are even better when the independent ECMWF analyses are used as reference field in the statistics, particularly at the 800 mb level.

- The analysis of the $RMSE_b$ vertical profiles obtained when radiosondes are used as reference field indicates that the assimilation of TR, alone or in combination with MW, has a small positive impact, compared with assimilation of CO only, on the 3- and 6-hr RH forecasts in the middle atmosphere from about 850 to about 350 hPa. Moreover, a small positive impact is also found in the 3-hr temperature forecast at the highest atmospheric levels (100–200 hPa) where a warm bias is often found in the model initial conditions when compared to observational data.

7. Discussion

This paper presents an advancement of the methodology previously introduced in A2020 toward the goal of efficiently assimilating hyperspectral data in NWP models. The approach introduced by Migliorini, provides the NWP centers with highly compressed, instrument-independent representations of the hyperspectral observations. Once the diagnostic system is equipped with the TR assimilation module, assimilation of TRs is seemingly easier and more computationally efficient than radiance assimilation. In fact: (a) it is more akin to assimilation of physical profiles while overcoming the errors introduced by using an a priori knowledge of the atmospheric state in the physical retrieval process (Eyre, 2007; Eyre et al., 2019) and(b) it does not seem to require bias correction.

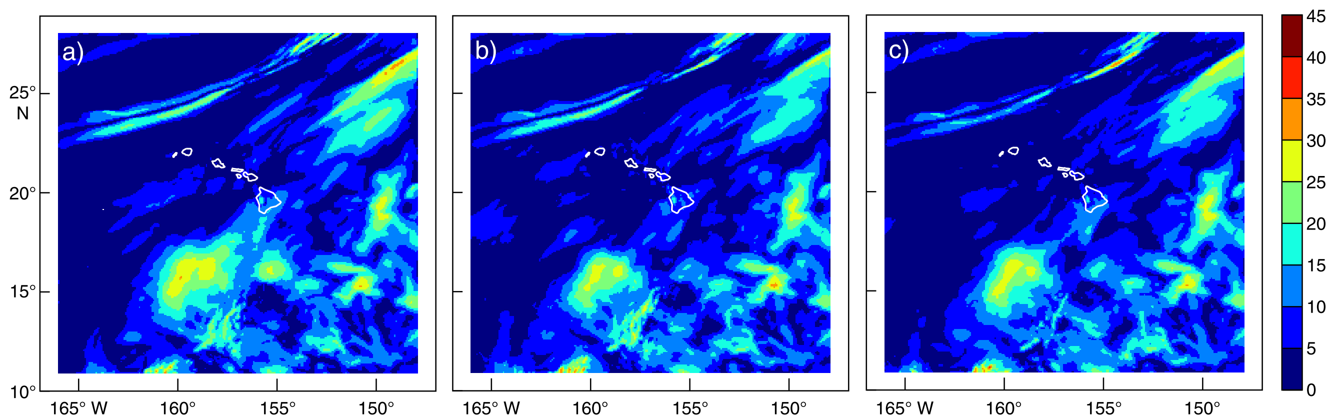

Figure 19. $RMSE_b$ for the 3-hr 600 mb relative humidity forecasts started at 09:00 UTC in the timeframe spanning from 02 December to 5 December (fifth cycle) when the European Centre for Medium-Range Weather Forecasts is used as reference field in the statistics for experiment: (a) CO; (b) Transformed Retrieval; and (c) TRMW.

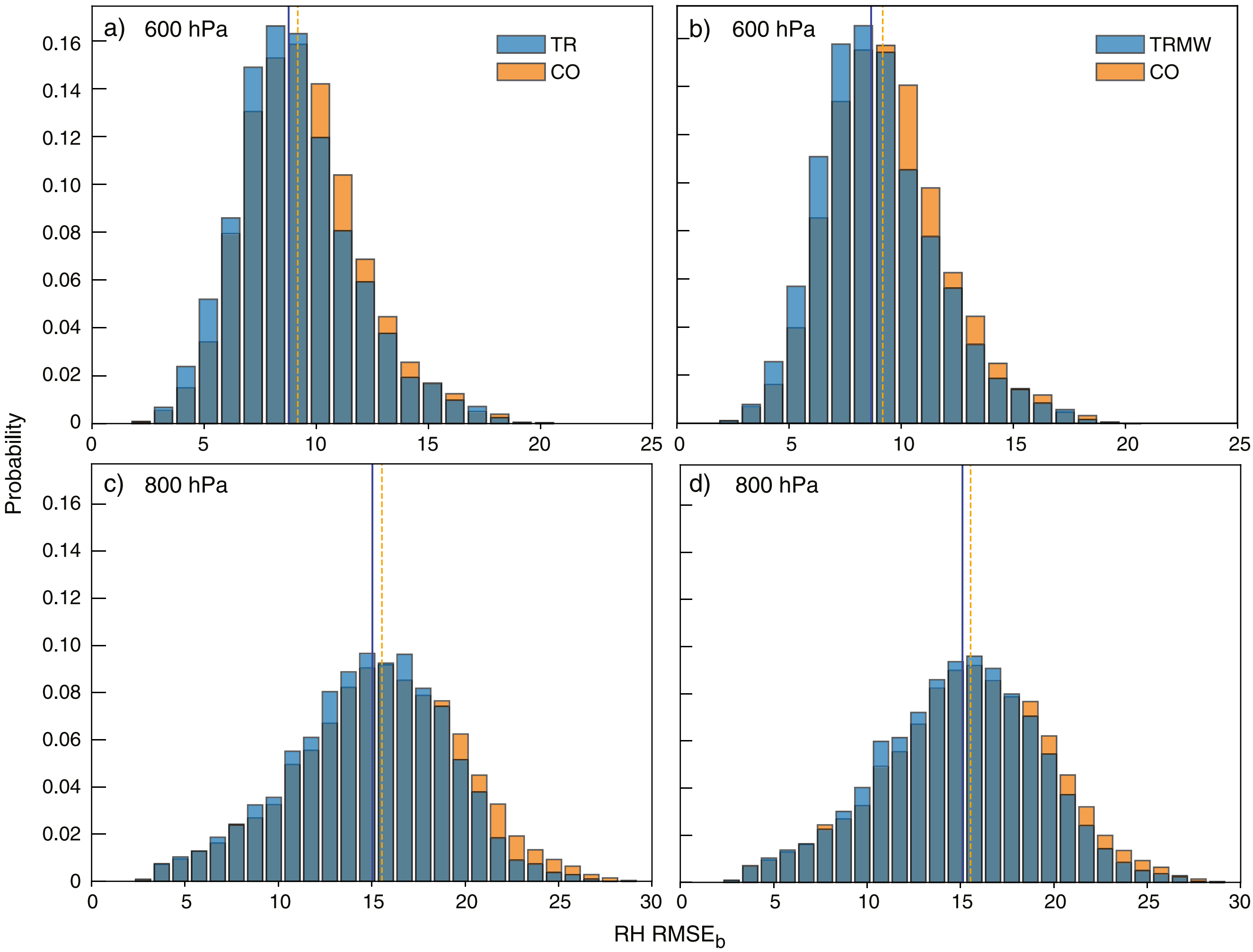

Figure 20. Relative humidity $RMSE_b$ distribution for the 3-hr forecasts started at 09:00 UTC throughout the entire experiment (20 November to 20 December 2020) at 600 hPa, when the Global Forecasting System is used as reference field in the statistics: (a) comparison between Transformed Retrieval (TR) and CO at 600 hPa; (b) comparison between TRMW and CO at 600 hPa; (c) comparison between TR and CO at 800 hPa; and (d) comparison between TRMW and CO at 800 hPa.

The month-long experiments show a positive dominant impact of the TRs on the forecast accuracy, which can be explained by the underlying amount of information provided by the TRs: the information content contained in thousands of channels from the hyperspectral sensors is highly and efficiently compressed into a limited number of uncorrelated parameters. On the other hand, MW radiances, although available in larger numbers in terms of FOVs, underlie a small number or satellite channels, that are likely correlated, because of their broad and overlapping weighting functions. Nevertheless, because of the lack of TRs information in cloudy area (so far), assimilation of MW radiances can prove complementary to TRs assimilation for those cases where cloud coverage can be an issue. The combination of IR TR and MW radiances seems to confirm their complementary nature in terms of spatial coverage, vertical resolution, and cloud impact mitigation. Having Mirto soundings available over the clouds would add additional useful information to the forecast system. Both the assimilation of TRs and MWs results in a higher forecast accuracy in predicting the distribution of the water vapor in the middle atmosphere. The assimilation of TRs improves the model performance in the lower portion of the middle atmosphere (800–700 hPa) and this is an even clearer takeaway from the statistical analysis carried out against the ECMWF analyses. An increased model performance against higher resolution analyses (ECMWF) points out to better custom WRDA analyses. Smaller scale moisture structures that would be smoothed out by the coarser GFS analyses resolution are captured instead. Validation against ECMWF analyses, compared to GFS analyses, show similar gains in the middle/higher levels of the atmosphere, as meteorological fields are naturally smoother in the free atmosphere, being further removed from the effects of turbulence induced by surface friction. However, a

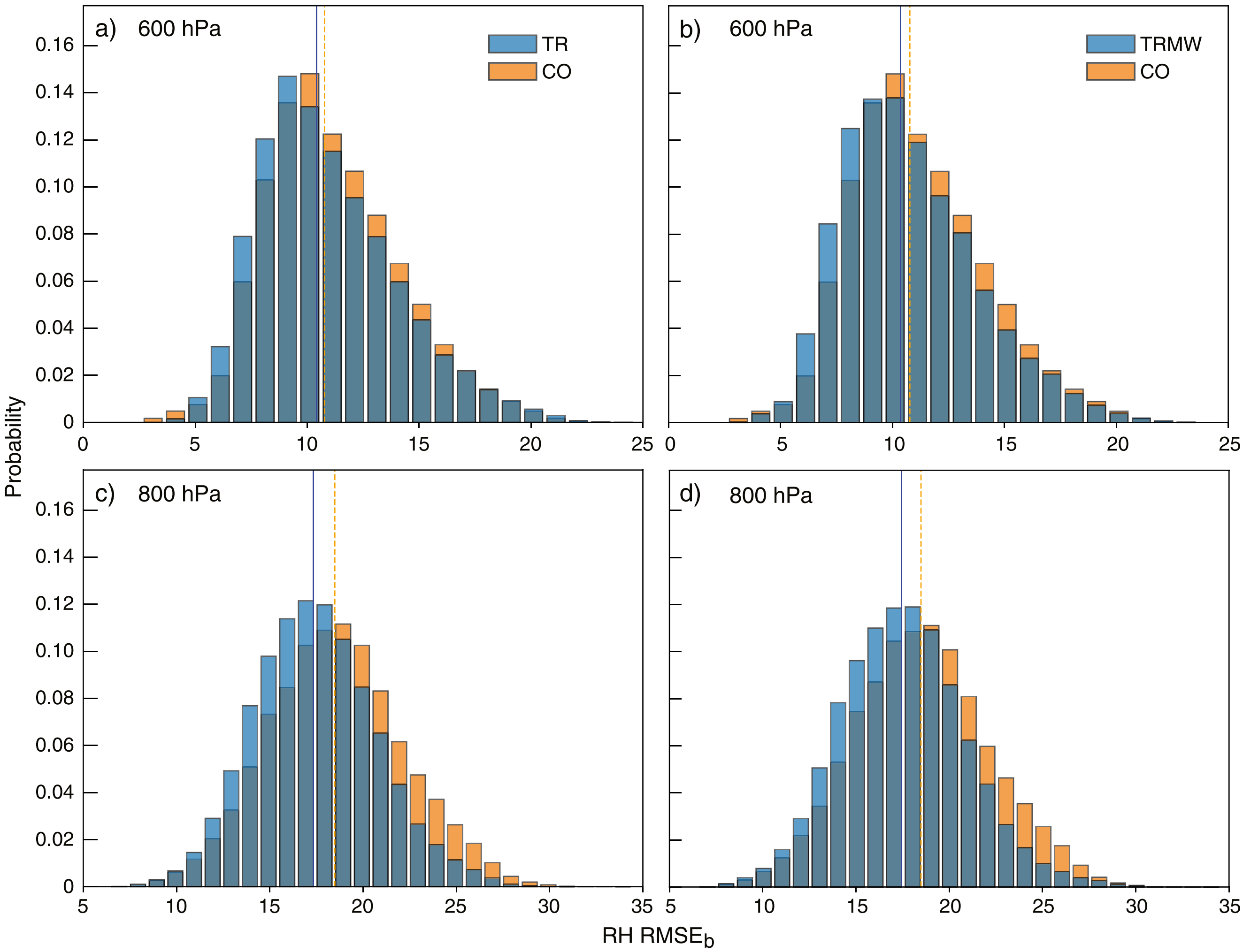

Figure 21. Figure 20. Relative humidity RMSE$_b$ distribution for the 3-hr forecasts started at 09:00 UTC throughout the entire experiment (20 November to 20 December 2020) at 600 hPa, when the European Centre for Medium-Range Weather Forecasts is used as reference field in the statistics: (a) comparison between Transformed Retrieval (TR) and CO at 600 hPa; (b) comparison between TRMW and CO at 600 hPa; (c) comparison between TR and CO at 800 hPa; and (d) comparison between TRMW and CO at 800 hPa.

better placement of the trade wind inversion in the lower portion of the middle atmosphere is indicated. This latter is particularly important for the central North Pacific region for several reasons: (a) a strong trade wind inversion inhibits deep convection formation of thunderstorms and tropical cyclones, therefore advanced knowledge of the tradewind inversion placement is very important in forecasting; (b) the trade wind inversion height and strength is correlated with rainfall intensity and distribution, particularly on the windward slopes of the Hawaiian islands (Esteban & Chen, 2008); and (c) an accurate prediction of the trade wind inversion height provides helpful guidance to the MKWC forecaster in assessing the weather at the summit of Maunakea (Lyman et al., 2020).

Hyperspectral instruments on polar orbiting satellites provide global coverage with high spatial and temporal resolution and can be an important resource for regions where conventional observations are lacking, such as over the open ocean and the Arctic. In fact, these data are widely assimilated in the NWP (Baker et al., 2005). Research shows that the ECMWF forecast errors are largest over the Arctic and far fewer MW observations are assimilated during winter than in summer in the ECMWF system, especially in regions covered by snow and sea ice (Lawrence et al., 2019). TR assimilation holds particular promise in these data sparse areas of the globe. The authors of this study are currently pursuing operational implementation of the WRF cycling system with TR and MW assimilation both over the Pacific and the Arctic. Another area of active research is calculation and assimilation of TRs in cloudy regions, which will be particularly important over the Arctic. A future goal is to make

TR assimilation available to other operational models such as NCEP's GFS and the Navy's new Neptune model through implementation in the JEDI framework (https://www.jcsda.org/jcsda-project-jedi).

Results described in this paper represent a forward step toward an efficient way to handle the assimilation of current (polar) and future (polar and geostationary) high-resolution IR instruments. It also shows how TRs assimilation can be effectively performed alongside the assimilation of other observations (conventional or MW).

Data Availability Statement

What follows is a description of the data used in this manuscript. Conventional Observations (CO) are PREBUFR format data available in real time via the NCEP web-server (National Centers for Environmental Prediction et al., 2008) and archived as NCEP ADP Global Upper Air and Surface Weather Observations, at the Research Data Archive (RDA) at the National Center for Atmospheric Research (NCAR), Computational and Information Systems Laboratory (CISL), Boulder, CO. Microwave radiance data (MW) in BUFR format are available in real time via the NCEP web server (National Centers for Environmental Prediction et al., 2009) and archived as NCEP GDAS Satellite Data, in BUFR format at the RDA (NCAR, CISL), Boulder, CO. The European Centre for Medium-Range Weather Forecasts (European Centre for Medium-Range Weather Forecasts, 2016) Integrated Forecast System (IFS) CY41r2 High-Resolution Operational Analysis and Forecasts are archived at the NCAR/CISL, Boulder, CO. The GFS analyses and forecasts are available in real time via the NCEP web-server (National Centers for Environmental Prediction et al., 2015) and archived as NCEP GFS 0.25° global forecast grids historical archive at the RDA (NCAR, CISL), Boulder, CO. The Level 1 data from both CrIS (Han et al., 2012) and IASI sensors (EUMETSAT/NESDIS, 2007), along with VIIRS (NOAA National Centers for Environmental Information, 2013) data are available from the NOAA, Comprehensive Large Array-data Stewardship System (CLASS). Radiosonde data are available online at the Dept. of Atmospheric Sciences of the University of Wyoming and College of Engineering (2022). Some figures were made with matplotlib version 3+ (Hunter, 2007), available under the matplotlib license at https://matplotlib.org/. Other figures were made with Matlab version 2022b, Natick, Massachusetts: The mathworks Inc. Maps were created using Cartopy, version v0.21.1 (Met Office, 2015). Part of the software (version 1.0.0) associated with this manuscript for the calculation of the presented statistics is licensed under the MIT license and available on GitHub/Zenodo, https://doi.org/10.5281/zenodo.7972524.

Acknowledgments
Thanks go to Nancy Hulbirt for help with the figures and May Izumi for her support to the manuscript editing. We acknowledge high-performance computing support from Cheyenne (https://doi.org/10.5065/D6RX99HX) provided by NCAR's Computational and Information Systems Laboratory (CISL), sponsored by the National Science Foundation. We thank the Research Data Archive (CISL) for conventional MW radiance observations, GFS and ECMWF analyses and forecast data, and the NOAA CLASS archive for CrIS, VIIRS, and IASI level 1 data availability. We would also like to acknowledge the Cooperative Institute for Meteorological Satellite Studies (CIMSS) for their Community Satellite Processing Package (CSPP), which was used to process all the data into EDRs and Level1C. This research was supported by the Office of Naval Research under ONR Award N00014-18-1-2166 and the Maunakea Support Services - Weather Center, Acct 0010390.

References

Antonelli, P., Cherubini, T., Auligné, T., Bernardini, L., Businger, S., & Marzano, F. (2015). *The potential of METEOSAT Third Generation (MTG) InfraRed Sounder (IRS) level 2 product assimilation in a very short-range numerical weather forecast model* (p. 79). EUMETSAT Final Rep.

Antonelli, P., Cherubini, T., Businger, S., de Haan, S., Scaccia, P., & Moncet, J. (2020). Regional assimilation system for transformed retrievals from satellite high-resolution infrared data. *Journal of Applied Meteorology and Climatology*, *59*(7), 1171–1193. https://doi.org/10.1175/JAMC-D-19-0203.1

Antonelli, P., Cherubini, T., Lyman, R., Giuliani, G., Revercomb, H., Businger, S., et al. (2017). Regional retrieval processor for direct broadcast high-resolution infrared data. *Journal of Applied Meteorology and Climatology*, *56*(6), 1681–1705. https://doi.org/10.1175/JAMC-D-16-0144.1

Auligné, T. (2007). An objective approach to modeling biases in satellite radiance assimilation: Application to AIRS and AMSU-A. *Quarterly Journal of the Royal Meteorological Society*, *133*(628), 1789–1801. https://doi.org/10.1002/qj.145

Auligné, T., & McNally, A. P. (2007). Interaction between bias correction and quality control. *Quarterly Journal of the Royal Meteorological Society*, *133*(624), 643–653. https://doi.org/10.1002/qj.57

Auligné, T., McNally, A. P., & Dee, D. P. (2007). Adaptive bias correction for satellite data in a numerical weather prediction system. *Quarterly Journal of the Royal Meteorological Society*, *133*(624), 631–642. https://doi.org/10.1002/qj.56

Baker, N. L., Hogan, T. F., Campbell, W. F., Pauley, R. L., & Swadley, S. D. (2005). *The impact of AMSU-A radiance assimilation in the U.S. Navy's operational global atmospheric prediction system (NOGAPS)* (p. 22). Marine Meteorology Division, Naval Research Laboratory, Memo. NRL/MR/7530–05-8836.

Barker, D. M., Huang, W., Guo, Y.-R., Bourgeois, A. J., & Xiao, Q. N. (2004). A three-dimensional variational data assimilation system for MM5: Implementation and initial results. *Monthly Weather Review*, *132*(4), 897–914. https://doi.org/10.1175/1520-0493(2004)132<0897:atvdas>2.0.co;2

Barker, D. M., Huang, X. Y., Liu, Z., Auligné, T., Zhang, X., Rugg, S., et al. (2012). The weather research and forecasting model's community variational/ensemble data assimilation system: WRFDA. *Bulletin of the American Meteorological Society*, *93*(6), 831–843. https://doi.org/10.1175/BAMS-D-11-00167.1

Businger, S., McLaren, R., Ogasawara, R., Simons, D., & Wainscoat, R. J. (2002). Starcasting. *Bulletin of the American Meteorological Society*, *83*(6), 858–871. https://doi.org/10.1175/1520-0477(2002)083,0858:S.2.3.CO;2

Cherubini, T., Businger, S., & Lyman, R. (2011). An operational perspective for modeling optical turbulence. In S. Businger & T. Cherubini (Eds.), *Seeing clearly: The impact of atmospheric turbulence on the propagation of extraterrestrial radiation* (pp. 165–182). VBW Publishing.

Cherubini, T., Businger, S., Velden, C., & Ogasawara, R. (2006). The impact of satellite-derived atmospheric motion vectors on mesoscale forecasts over Hawaii. *Monthly Weather Review*, *134*(7), 2009–2020. https://doi.org/10.1175/MWR3163.1

Cherubini, T., Lyman, R., & Businger, S. (2021). Forecasting seeing for the Maunakea observatories with machine learning. *Monthly Notices of the Royal Astronomical Society*, *509*(1), 232–245. https://doi.org/10.1093/mnras/stab2916

Corrigan, T. J., & Businger, S. (2021). The anatomy of a series of cloud bursts that eclipsed the U.S. rainfall record. *Monthly Weather Review*, *150*(4), 753–773. https://doi.org/10.1175/MWR-D-21-0028.1

Cucurull, L., & Anthes, R. A. (2014). Impact of infrared, microwave, and radio occultation satellite observations on operational numerical weather prediction. *Monthly Weather Review*, *142*(11), 4164–4186. https://doi.org/10.1175/MWR-D-14-00101.1

Dee, D. P. (2005). Bias and data assimilation. *Quarterly Journal of the Royal Meteorological Society*, *131*(613), 3323–3343. https://doi.org/10.1256/qj.05.137

DeHaan, S., Marseille, G.-J., & De Valk, P. (2015). *The potential of METEOSAT Third Generation (MTG) InfraRed Sounder (IRS) level 2 product assimilation in a very short range numerical weather forecast model*. Technical Report. EUMETSAT.

Dept. of Atmospheric Sciences at University of Wyoming, & College of Engineering. (2022). Dept. of atmospheric Sciences [Dataset]. http://weather.uwyo.edu/upperair/sounding.html

Dudhia, J. (1989). Numerical study of convection observed during the winter monsoon experiment using a mesoscale two-dimensional model. *Journal of the Atmospheric Sciences*, *46*(20), 3077–3107. https://doi.org/10.1175/1520-0469(1989)046<3077:NSOCOD>2.0.CO;2

Esteban, M. A., & Chen, Y.-L. (2008). The impact of trade wind strength on precipitation over the windward side of the Island of Hawaii. *Monthly Weather Review*, *136*(3), 913–928. https://doi.org/10.1175/2007MWR2059.1

EUMETSAT/NESDIS. (2007). *European organisation for the exploitation of meteorological satellites. Infrared atmospheric sounding interferometer (IASI) level 1C data*. NESDIS, NOAA, U.S. Department of Commerce. Retrieved from www.ncdc.noaa.gov

European Centre for Medium-Range Weather Forecasts. (2016). ECMWF IFS CY41r2 High-resolution operational forecasts (updated monthly) [Dataset]. Research Data Archive at the National Center for Atmospheric Research, Computational and Information Systems Laboratory. https://doi.org/10.5065/D68050ZV

Eyre, J. R. (2007). Progress achieved on assimilation of satellite data in numerical weather prediction over the last 30 years. In *Seminar on recent developments in the use of satellite observations in numerical weather prediction*. ECMWF. Retrieved from https://www.ecmwf.int/sites/default/files/elibrary/2008/9341-progress-achieved-assimilation-satellite-data-numerical-weather-prediction-over-last-30-years.pdf

Eyre, J. R. (2016). Observation bias correction schemes in data assimilation systems: A theoretical study of some of their properties. *Quarterly Journal of the Royal Meteorological Society*, *142*(699), 2284–2291. https://doi.org/10.1002/qj.2819

Eyre, J. R., English, S. J., & Forsythe, M. (2019). Assimilation of satellite data in numerical weather prediction. Part I: The early years. *Quarterly Journal of the Royal Meteorological Society*, *146*(726), 49–68. https://doi.org/10.1002/qj.3654

Han, Y., Qiu, S., Shuang, & NOAA JPSS Program Office. (2012). NOAA JPSS cross-track infrared sounder (CrIS) science sensor data record (SDR) from IDPS. JPSS-CrIS-SDR [Dataset]. NOAA National Centers for Environmental Information. https://doi.org/10.7289/V59C6VGK

Haseler, J. (2004). Early-delivery suite. *ECMWF Technical Memoranda*, *454*. https://doi.org/10.21957/f3wtwz0h

Hong, S., & Lim, J. (2006). The WRF single-moment 6-class microphysics scheme (WSM6). *Asia-Pacific Journal of Atmospheric Sciences*, *42*, 129–151.

Hunter, J. D. (2007). Matplotlib: A 2D graphics environment. *Computing in Science & Engineering*, *9*(3), 90–95. https://doi.org/10.1109/MCSE.2007.55

Janjic, Z. I. (2002). Nonsingular implementation of the Mellor-Yamada level 2.5 scheme in the NCEP meso model, NCEP Office Note (No. (437), p. 61). Retrieved from https://repository.library.noaa.gov/view/noaa/11409

Joiner, J., & Da Silva, A. (1998). Efficient methods to assimilate remotely sensed data based on information content. *Quarterly Journal of the Royal Meteorological Society*, *124*(549), 1669–1694. https://doi.org/10.1002/qj.49712454915

Lawrence, H., Bormann, N., Sandu, I., Day, J., Farnan, J., & Bauer, P. (2019). Use and impact of Arctic observations in the ECMWF numerical weather prediction system. *Quarterly Journal of the Royal Meteorological Society*, *145*(725), 3432–3454. https://doi.org/10.1002/qj.3628

Lean, P., Holm, E. V., Bonavita, M., Bormann, N., McNally, A. P., & Jarvinen, H. (2020). Continuous data assimilation for global numerical weather prediction. *Quarterly Journal of the Royal Meteorological Society*, *147*(734), 273–288. https://doi.org/10.1002/qj.3917

Lyman, R., Cherubini, T., & Businger, S. (2020). Forecasting seeing for the Maunakea observatories. *Monthly Notices of the Royal Astronomical Society*, *496*(4), 4734–4748. https://doi.org/10.1093/mnras/staa1787

Matricardi, M., & McNally, A. P. (2014). The direct assimilation of principal components of IASI spectra in the ECMWF 4D-Var. *Quarterly Journal of the Royal Meteorological Society*, *140*(679), 573–582. https://doi.org/10.1002/qj.2156

McNally, A. (2009). The direct assimilation of cloud-affected satellite infrared radiances in the ECMWF 4D-Var. *Quarterly Journal of the Royal Meteorological Society*, *135*(642), 1214–1229. https://doi.org/10.1002/qj.426

Met Office. (2015). Cartopy: A cartographic python library with a Matplotlib interface (2010-2015) [Software]. https://doi.org/10.5281/zenodo.1182735

Migliorini, S. (2012). On the equivalence between radiance and retrieval assimilation. *Monthly Weather Review*, *140*(1), 258–265. https://doi.org/10.1175/MWR-D-10-05047.1

Migliorini, S., Piccolo, C., & Rodgers, C. (2008). Use of the information content in satellite measurements for an efficient interface to data assimilation. *Monthly Weather Review*, *136*(7), 2633–2650. https://doi.org/10.1175/2007MWR2236.1

Mlawer, E. J., Taubman, S. J., Brown, P. D., Iacono, M. J., & Clough, S. A. (1997). Radiative transfer for inhomogeneous atmosphere: RRTM, a validated correlated-k model for the longwave. *Journal of Geophysical Research*, *102*(D14), 16663–16682. https://doi.org/10.1029/97jd00237

National Centers for Environmental Prediction, National Weather Service, NOAA, & U.S. Department of Commerce. (2008). NCEP ADP global upper air and surface weather observations (PREPBUFR format) [Dataset]. Research Data Archive at the National Center for Atmospheric Research, Computational and Information Systems Laboratory. https://doi.org/10.5065/Z83F-N512

National Centers for Environmental Prediction, National Weather Service, NOAA, & U.S. Department of Commerce. (2009). NCEP GDAS satellite data 2004-continuing [Dataset]. Research Data Archive at the National Center for Atmospheric Research, Computational and Information Systems Laboratory. https://doi.org/10.5065/DWYZ-Q852

National Centers for Environmental Prediction, National Weather Service, NOAA, & U.S. Department of Commerce. (2015). NCEP GFS 0.25 degree global forecast grids historical archive [Dataset]. Research Data Archive at the National Center for Atmospheric Research, Computational and Information Systems Laboratory. https://doi.org/10.5065/D65D8PWK

NOAA National Centers for Environmental Information. (2013). VIIRS climate raw data record (C-RDR) from Suomi NPP, version 1. NCEI DSI 3658_01 [Dataset]. NOAA National Centers for Environmental Information. https://doi.org/10.7289/V57P8W90

Ochotta, T., Cebhardt, C., Saupe, D., & Wergen, W. (2005). Adaptive thinning of atmospheric observations in data assimilation with vector quantization and filtering methods. *Quarterly Journal of the Royal Meteorological Society*, *131*(613), 3427–3437. https://doi.org/10.1256/qj.05.94

Rodgers, C. (2000). *Inverse methods for atmospheric soundings: Theory and practice* (p. 238). World Scientific.

Simmons, A. J., & Hollingsworth, A. (2002). Some aspects of the improvement in skill of numerical weather prediction. *Quarterly Journal of the Royal Meteorological Society*, *128*(580), 647–677. https://doi.org/10.1256/003590002321042135

Skamarock, W. C., Klemp, J. B., Dudhia, J., Gill, D. O., Barker, D., Duda, M. G., et al. (2008). *A description of the advanced research WRF version 3 (No. NCAR/TN-475+STR)*. University Corporation for Atmospheric Research. https://doi.org/10.5065/D68S4MVH

Wang, Y., He, J., Chen, Y., & Min, J. (2021). The potential impact of assimilating synthetic microwave radiances onboard a future geostationary satellite on the prediction of Typhoon Lekima using the WRF model. *Remote Sensing*, *13*(5), 886. https://doi.org/10.3390/rs13050886

Weng, F., Han, Y., Van Delst, P., Liu, Q., & Yan, B. (2005). JCSDA community radiative transfer model (CRTM). In *Proc. 14th int. ATOVS study conf.* (pp. 217–222).

Zapotocny, T. H., Jung, J. A., Le Marshall, J. F., & Treadon, R. E. (2008). A two-season impact study of four satellite data types and rawinsonde data in the NCEP Global Data Assimilation System. *Weather and Forecasting*, *23*(1), 80–100. https://doi.org/10.1175/2007waf2007010.1

Zhang, C., & Wang, Y. (2017). Projected future changes of tropical cyclone activity over the western North and South Pacific in a 20-km-mesh regional climate model. *Journal of Climate*, *30*(15), 5923–5941. https://doi.org/10.1175/JCLI-D-16-0597.1